



## Volatile budgets and evolution in porphyry-related magma systems, determined using apatite

Charline Lormand<sup>a,\*</sup>, Madeleine C.S. Humphreys<sup>a</sup>, David J. Colby<sup>a</sup>, Jason P. Coumans<sup>a</sup>, Cyril Chelle-Michou<sup>b</sup>, Weiran Li<sup>c</sup>

<sup>a</sup> Department of Earth Sciences, Durham University, UK

<sup>b</sup> Department of Earth Sciences, ETH, Zürich, Switzerland

<sup>c</sup> Department of Earth Sciences, The University of Hong Kong, Hong Kong

### ARTICLE INFO

#### Keywords:

Apatite  
Volatiles  
Porphyry Cu deposits  
Halogens  
Fluid salinity

### ABSTRACT

Volatile-bearing minerals, such as apatite,  $\text{Ca}_5(\text{PO}_4)_3(\text{OH},\text{F},\text{Cl})$ , can record changes in dissolved magmatic volatile species during differentiation and, unlike melt inclusions, are sensitive to the presence of an exsolved fluid phase. Populations of apatite crystals from an individual sample can therefore be used to define the progressive volatile evolution of melt  $\pm$  fluid during magma differentiation. Despite the importance of fluid chemistry in mineralisation processes, this approach remains relatively underdeveloped for porphyry mineralisation scenarios. Here, we present a model, including a standalone MATLAB app, for melt + apatite  $\pm$  fluid fractionation that incorporates non-ideal, temperature-dependent  $K_{\text{DS}}$  for OH-Cl-F exchange and permits an analysis of uncertainty arising from non-unique parameter combinations. We apply the model to apatite from the Fe-Cu-Au Corrocohuayco porphyry-skarn system and analyse differences in volatile saturation state and fluid salinity between different units. We find that there is little difference in the overall fluid salinity, and thus the fluid copper loads, but that the more primitive unit (i.e. the gabbrodiorites) reached fluid saturation much later (after around 50% crystallisation) than the more evolved units, implying that the melt volatile concentration recorded by the apatites in the gabbrodiorites is not representative of the initial magma volatile budget. This work demonstrates that apatite can be a good alternative means of reconstructing the evolving magmatic fluid salinity within mineralising systems, and linking this to the trace metal content of the melt.

## 1. Introduction

### 1.1. Volatiles in magmas and apatite

Dissolved magmatic volatiles in melts influence the abundance and chemistry of minerals growing from a melt, as well as the density and viscosity of the evolving magma. Exsolution of those volatiles into a free gas or fluid phase that expands during ascent is a critical part of most eruption pathways. The compositions, abundances and degassing of volatiles (i.e.  $\text{H}_2\text{O}$ ,  $\text{CO}_2$ ,  $\text{SO}_2$ , halogens) from the melt have a key influence on the resulting eruption style of volcanoes (e.g. Blake, 1984). Furthermore, the behaviour of volatiles around the magmatic-hydrothermal transition has a critical control on the compositions of mineralising systems (e.g., Kouzmanov and Pokrovski, 2012; Lecumberri-Sanchez and Bodnar, 2018).

Analytical techniques to measure the volatile content of magmas include in-situ analysis of mineral-hosted melt and fluid inclusions (e.g. Bodnar et al., 2014; Metrich and Clochchiatti, 1989; Pamukcu et al., 2015) as they can provide direct evidence of the initial volatile budget of magmas before volatile exsolution during decompression (i.e. first boiling), and cooling and crystallisation (i.e. second boiling). However, due to potential re-equilibration and/or post-entrapment crystallisation, melt inclusions are not always representative of the volatile content at magmatic conditions (e.g. Brahm et al., 2021; Gavrilenko et al., 2019). Fluid inclusions form throughout the evolution of magmas, from early crystallisation until late-stage crystallisation for instance at the magmatic-hydrothermal transition, and thus may record multiple processes, making them challenging to interpret, especially for multicomponent fluids containing halogens (e.g. Evans and Tomkins, 2020). Halogen contents in mineral phases have been used to infer halogen

\* Corresponding author at: Department of Earth Sciences, University of Geneva, Switzerland.

E-mail addresses: [charline.lormand@unige.ch](mailto:charline.lormand@unige.ch) (C. Lormand), [madeleine.humphreys@durham.ac.uk](mailto:madeleine.humphreys@durham.ac.uk) (M.C.S. Humphreys), [david.j.colby@durham.ac.uk](mailto:david.j.colby@durham.ac.uk) (D.J. Colby), [coumansj87@gmail.com](mailto:coumansj87@gmail.com) (J.P. Coumans), [cyril.chelle-michou@erdw.ethz.ch](mailto:cyril.chelle-michou@erdw.ethz.ch) (C. Chelle-Michou), [weiranli@hku.hk](mailto:weiranli@hku.hk) (W. Li).

<https://doi.org/10.1016/j.lithos.2024.107623>

Received 4 January 2024; Received in revised form 26 April 2024; Accepted 26 April 2024

Available online 5 May 2024

0024-4937/© 2024 The Authors. Published by Elsevier B.V. This is an open access article under the CC BY-NC-ND license (<http://creativecommons.org/licenses/by-nc-nd/4.0/>).

concentrations of the mantle (e.g. Gibson et al., 2020) but such studies use nominally anhydrous minerals (e.g. clinopyroxene and olivine) that only contain trace amounts of volatiles whose partition behaviour is thus treated as Nernstian. In the case of hydrous minerals (e.g. amphibole and apatite), the volatiles are required components of the mineral structure where exchange coefficients ( $K_D$ s) are more appropriate to describe the partitioning behaviour.

Thanks to phase equilibrium experiments and thermodynamic datasets available in the literature, volatile-bearing minerals (e.g. biotite, amphibole, apatite) now offer more avenues to access the volatile content of magmas (e.g. Giesting and Filiberto, 2014; Hammouda et al., 2010; Humphreys et al., 2021; Li et al., 2021; Stock et al., 2018; Watson and Green, 1981; Zajacz et al., 2012). Apatite [ $\text{Ca}_5(\text{PO}_4)_3(\text{OH}, \text{F}, \text{Cl})$ ] can incorporate water, fluorine and chlorine into its crystal structure through non-ideal mixing of these volatiles on the channel site, which can be described by a series of exchange equilibria linking the volatile compositions of apatite to those of the melt (e.g. Candela, 1986; Li and Costa, 2020, 2023; Stock et al., 2016, 2018). Therefore, apatite chemistry has increasingly been used to interpret the volatile evolution of magmas in both mineralising and volcanic systems (e.g. Bernard et al., 2022; Boudreau, 1995; Boyce and Hervig, 2008; Humphreys et al., 2021; Li et al., 2020a, 2020b; Piccoli and Candela, 1994; Riker et al., 2018; Scott et al., 2015; Stock et al., 2016). Apatite has been found to crystallise in diverse melt compositions from basaltic andesite to phonolite, over a range of pressures and temperatures (i.e. from upper mantle conditions to the Earth's surface and from 1200 °C to <650 °C; e.g. Boudreau and McCallum, 1989; Harrison and Watson, 1984; Piccoli and Candela, 1994; Stock et al., 2016). Apatite may occur as mineral-hosted inclusions (in amphibole e.g. Chelle-Michou and Chiaradia, 2017, Li et al., 2021; in biotite e.g. Stock et al., 2016; in plagioclase e.g. Humphreys et al., 2006; in zircon e.g., Nathwani et al., 2023; in clinopyroxene, Krause et al., 2013) as well as microphenocrysts or microlites in volcanic rocks and as interstitial crystals in plutonic rocks. This versatility allows the evolution of volatile concentration in the melt to be tracked from early crystallisation to volatile exsolution and beyond (e.g. Fig. 2 of Stock et al., 2016; Humphreys et al., 2021; Popa et al., 2021).

### 1.2. Volatiles in porphyry-related magmatic-hydrothermal deposits

The behaviour of an exsolved volatile phase is critical to the development of porphyry-related mineral deposits (Heinrich, 2007; Kouzmanov and Pokrovski, 2012; Shinohara and Hedenquist, 1997), which are key sources of critical metals such as Cu, Mo, Au and Ag (e.g. Richards, 2015). Cu is the main metal for electrification for which the demands are projected to increase until at least 2060 (Schipper et al., 2018). Porphyry mineralisation occurs when exsolved, metal-bearing fluids are efficiently channelled from crystallising intrusions up into restricted regions of the upper crust (Lamy-Chappuis et al., 2020; Richards, 2022; Wilkinson, 2013), where they cool and precipitate metals in the form of sulphide minerals associated with copious hydrothermal alteration (Hedenquist and Lowenstern, 1994; Simon and Ripley, 2011). Multiple magmatic processes influence the delivery of magmatic-hydrothermal fluids into the upper crust, including the volume and overall duration of magmatism (Chelle-Michou and Chiaradia, 2017; Chiaradia and Caricchi, 2017; Schöpa et al., 2017), the volatile contents and composition of the initial melt (e.g. Hogg et al., 2023; Nathwani et al., 2023), the abundance and composition of the exsolving fluid (Chelle-Michou and Chiaradia, 2017), and the relative timing (and pressure) of fluid saturation relative to metal enrichment (Audétat, 2019; Chiaradia and Caricchi, 2017). Unusual fluid compositions may not be required if there is sufficient fluid volume (e.g. Audétat, 2019; Wilkinson, 2013) but metals must be abundantly available in the melt at the time of fluid saturation and exsolution (Hedenquist and Lowenstern, 1994; Simon and Ripley, 2011). Both chlorine and sulphur are key elements to facilitate the transport of metal-bearing fluids to the site of ore deposition (Candela and Holland, 1984; Tattitch and Blundy, 2017), as

they can form ligands with both ore metals (e.g. Cu, Mo, Au, Fe, Pb, Zn) and other cations (e.g.  $\text{Ca}^{2+}$ ,  $\text{Na}^+$ ,  $\text{H}^+$ ,  $\text{K}^+$ ). However, significant questions remain over (1) whether abundant, low salinity fluids with low metal concentrations are more important than small volumes of more saline, more metal-rich fluids (Audétat, 2019), and (2) how fluid salinity and metal content vary during the history of magmatic degassing, with fluid inclusions ranging from ~2–25 wt%  $\text{NaCl}_{\text{eq}}$  (wt% - weight percent; Audétat et al., 2008; Kouzmanov and Pokrovski, 2012). Here, we aim at determining how porphyry mineralisation at the Corocchohuayco Fe-Cu-Au deposit, Peru, is impacted by the relative timing of fluid saturation, initial melt composition and fluid salinity, using independent constraints on the magmatic volatile record from modelling of apatite chemistry.

In this study, we focus on reinterpreting the apatite volatile geochemistry previously published by Chelle-Michou and Chiaradia (2017) to infer the timing of fluid saturation and reconstruct the salinity of fluids in equilibrium with apatite during crystallisation of each magmatic unit. We exploit the observation that apatite compositions can be well preserved, even in plutonic rocks, whereas amphibole compositions tend to be more easily reset and could be a less reliable record of dissolved volatiles (Humphreys et al., 2022). We build on recent work that uses populations of apatite to infer magmatic volatile evolution (Humphreys et al., 2021) and use improvements in thermodynamic understanding that demonstrate the importance of non-ideal partitioning of F, Cl, and OH within the apatite (Li and Costa, 2020, 2023). Our overarching aim is to recover more precise constraints on the initial melt volatile compositions, and to evaluate whether apatite composition can be used to accurately constrain the evolution of volatiles and exsolved fluids (e.g. timing of fluid saturation, relative concentrations of water and halogens) during fractionation in porphyry-forming systems.

## 2. Geological background: the Corocchohuayco FE-CU-AU porphyry-skarn magmatic suite

This work focusses on the Eocene Corocchohuayco Fe-Cu-Au porphyry-skarn system in southern Peru. This case study is ideal due to an abundance of apatite and the existing geological, geochemical, and mineral constraints on the system's evolution, which can be used to help interpret our modelling results. Chelle-Michou et al. (2014, 2015a, 2015b) have described the geochronology, the petrological and geochemical evolution of the Corocchohuayco magmatic suite whereas Chelle-Michou and Chiaradia (2017) focused on the volatile evolutions (i.e. Cl and S) recorded by the amphibole and apatite mineral phases. We summarise their findings hereafter.

The Corocchohuayco porphyry-skarn Cu deposit is located at the southern end of the Eocene Andahuaylas-Yauri calc-alkaline batholith in the Tintaya mining district of southern Peru (e.g. Chelle-Michou et al., 2015a). Magmatic activity started with the emplacement of a gabbrodiorite complex (GDC) at 40.5–40.2 Ma (Chelle-Michou et al., 2014) which consists of gabbrodiorite (10CC09, used here), gabbrodiorite cumulate, leuco-gabbrodiorite and subordinate anorthosite. The gabbrodiorite and the cumulate represent >95% in volume of the GDC and both contain normally zoned plagioclase ( $\text{An}_{90}\text{-An}_{30}$ ), poikilitic hornblende (hbl) surrounding resorbed pyroxene, magnetite, ilmenite and interstitial quartz  $\pm$  K-feldspar  $\pm$  biotite (Chelle-Michou et al., 2015a and Fig. 2a, b therein). The accessory minerals consist of apatite, zircon, titanite and magmatic sulfides. At 35.6 Ma, after a magmatic quiescence of c. 5 Ma, a major magmatic-hydrothermal event occurred and formed a hornblende-dacite porphyry and a hornblende-biotite-dacite porphyry associated with the Fe-Cu-Au porphyry-skarn mineralisation. These were crosscut by rhyodacite dykes (Chelle-Michou et al., 2015a; Chelle-Michou and Chiaradia, 2017) that have evidence of alteration of mafic minerals. The main mineral phases of the porphyries are hornblende, plagioclase ( $\text{An}_{30}\text{-An}_{10}$ ), magnetite, biotite and K-feldspar. Their matrix is microcrystalline and made of quartz, albitic plagioclase and K-feldspar, and they have the same accessory phases as the GDC (i.e. apatite,

zircon and titanite) but lack magmatic sulfides. The rhyodacite dykes show evidence of prevalent hydrothermal alteration of mafic minerals (i.e. amphibole and biotite), and plagioclases and the groundmass have often experienced variable degrees of sericitization (Chelle-Michou et al., 2015a).

Whole rock isotopic (i.e. age corrected Pb, Sr, and Nd isotopes) and geochemical data indicate that the Corocohuayco magmatic suite has a typical isotopic signature from subduction-related magmas (i.e. negative Nb, Ta and Ti anomalies and LILE enrichment) and their source is similar (Chelle-Michou et al., 2015a). However, the GDC was sourced from a heterogeneous deep crustal hot zone and formed a chemically zoned pluton, whereas the porphyry magmas were sourced from more homogeneous magma batches originating from lower to mid-crustal depths. Indeed, GDC has evidence of textural and mineralogical (i.e. micro-scale mingling between clinopyroxene-rich and orthopyroxene-rich magmas), as well as isotopic (i.e. variable Sr and Nd in the whole rock and variable Hf in zircons) heterogeneities (Chelle-Michou et al., 2015a). The porphyries, instead, have more homogeneous textural and isotopic compositions suggesting a more homogeneous source consisting of magma batches that have undergone various degrees of assimilation and fractionation, as well as partial melting of older magma batches and magma recharge (Chelle-Michou et al., 2015a).

Estimates of melt dissolved water concentrations determined using plagioclase-liquid hygrometry (Lange et al., 2009) for GDC and using hornblende hygrometry (Ridolfi and Renzulli, 2012) for the porphyries are about 3 wt% and 5 wt% respectively (Chelle-Michou et al., 2015a). Other volatile species (i.e. Cl and S) were previously measured in apatites and amphiboles to determine whether the volatile contents and composition of the pre-mineralisation GDC were different to those of the later porphyry magmas that resulted in porphyry-skarn mineralisation (Supplementary Material 1 in Chelle-Michou and Chiaradia, 2017). Preliminary estimations of melt halogen compositions inferred by Chelle-Michou and Chiaradia (2017) were calculated from: (i) apatite, using the partitioning model of Li and Hermann (2017) and the experimental data from Webster et al. (2009) at 200 MPa and 900 °C; and from (ii) amphibole, using the experimental calibration of Giesting and Filiberto (2014). The magmatic Cl concentrations retrieved from both minerals are within the range of Cl melt concentrations for arc magmas (0.01–0.85, Aiuppa et al., 2009) but they do not overlap: values calculated using apatite are about twice as high as those derived from amphibole (i.e. 0.6 wt% versus 0.37 wt% for the gabbrodiorites and 0.2 wt% versus 0.1 wt% for the porphyries using apatite and amphibole, respectively). Chelle-Michou and Chiaradia (2017) then used these melt reconstructions to infer fluid salinity  $\text{NaCl}_{\text{eq}}$  of 1–10 wt% using  $D_{\text{Cl}}^{\text{m-m}} = 4.5$  and 20 for pressures of 100 and 200 MPa, respectively (Zhang et al., 2012). However, the discrepancies between the melt Cl contents derived from apatite and amphibole raise questions about the accuracy of this approach. Intensive parameters such as melt  $\text{H}_2\text{O}$  content are poorly constrained: limited sensitivity testing suggested that melt  $\text{H}_2\text{O}$  relative error could be of  $\pm 15\%$  (Chelle-Michou and Chiaradia, 2017), but this seems conservative. Inferred storage pressures are in the (wide) range of 250–100 MPa which suggests that, for an initial melt with 5 wt%  $\text{H}_2\text{O}$ , the magma could have been initially either fluid-saturated or undersaturated. Conversely, it is possible that the differences in estimated halogen contents are related to real compositional changes in the melt between crystallisation of amphibole and apatite, as the textural evidence show that they grew concomitantly. Finally, the timing of fluid saturation relative to fractionation is important for understanding metal enrichment or depletion in the residual liquid (Audétat, 2019; Tattitch et al., 2021); this remains a key unknown for this system.

### 3. Modelling approach to volatiles in apatite

#### 3.1. Incorporating non-ideal partitioning for F, Cl, OH

We base our model for apatite  $\pm$  fluid fractionation on that developed by Humphreys et al. (2021), which calculates, for each increment of fractionation, (i) the volatile evolution in the melt and fluid (if any), (ii) the composition of the apatite in equilibrium with the melt, and (iii) the composition and mass of the fluid exsolved. Our approach is to use the model to fit a general fractionation trend to the whole apatite population for each unit or sample. This means that we treat the apatite compositions from each unit as representative of the shared P-T-X-t history of that magma. We prefer this approach to that of Nathwani et al. (2023), who essentially treat each apatite individually: their successful model runs are those that intercept any melt composition derived from any apatite, whereas ours must fit the whole population.

The model of Humphreys et al. (2021) assumed ideal mixing of OH-F-Cl in the apatite volatile site and used fixed (bulk) fluid-melt ( $D_{\text{f-m}}^{\text{f-m}}$ ) and bulk crystal-melt partition coefficients ( $D_{\text{c-m}}^{\text{c-m}}$ ). However, mixing has been shown to be non-ideal (Li and Costa, 2020, 2023), and this is more prominent at lower temperatures. The non-ideality is due to different interactions between the  $\text{OH}^-$ ,  $\text{F}^-$  and  $\text{Cl}^-$  anions and their neighbouring atoms i.e. Ca and O (e.g. Hughes et al., 2014), resulting from the difference in ionic radius (Shannon and Prewitt, 1969) and different anion positions in the apatite anion column (Hughes, 2015). The  $K_{\text{DS}}$  can also vary substantially with temperature, especially at typical magmatic temperatures (Fig. 6 of Li and Costa, 2020, 2023). Therefore, we have updated and improved the model by incorporating the T-X-dependent  $K_{\text{DS}}$  following the regression of Li and Costa (2020, 2023) defined as:

$$\ln\left(K_{D_{\text{OH-F}}}^{\text{Ap-melt}}\right) = -\frac{1}{RT} \times \{94,600(\pm 5600) - 40(\pm 0.1) \times T + 1000 \times [7(\pm 4) \times (X_{\text{F}}^{\text{Ap}} - X_{\text{OH}}^{\text{Ap}}) - 11(\pm 7) \times X_{\text{Cl}}^{\text{Ap}}]\} \quad (1)$$

and

$$\ln\left(K_{D_{\text{OH-Cl}}}^{\text{Ap-melt}}\right) = -\frac{1}{RT} \times \{72,900(\pm 2900) - 34(\pm 0.3) \times T + 1000 \times [5(\pm 2) \times (X_{\text{Cl}}^{\text{Ap}} - X_{\text{OH}}^{\text{Ap}}) - 10(\pm 8) \times X_{\text{F}}^{\text{Ap}}]\} \quad (2)$$

where the temperature T is in Kelvins, the apatite composition  $X_{\text{i}}^{\text{Ap}}$  is in mole fraction and R is the universal gas constant.

The temperature is either fixed or can be taken from a relationship between temperature and melt fraction if this is well known and can be determined using petrological constraints. In the case of the Corocohuayco suite, previous temperature estimates from amphibole thermometry gave a range between 750 °C and 1000 °C, and the most likely crystallisation temperatures of apatite for the gabbrodiorites and the porphyries are 850–800 °C and 900–850 °C, respectively (Chelle-Michou and Chiaradia, 2017). The lower temperature for apatite crystallisation in the gabbrodiorites arises because apatite forms late in the fractionation sequence and is always either included in interstitial amphibole, or in other late interstitial spaces (Chelle-Michou and Chiaradia, 2017). For consistency with the former studies, we modelled the apatite fractionation at 850 °C for the gabbrodiorites and at 900 °C for the porphyries and rhyodacite.

#### 3.2. Our approach to modelling

To model the apatite trends, we first use an understanding of the effects of changing the individual parameters (i.e. initial melt volatile composition, i.e. Cl, F and  $\text{H}_2\text{O}$  concentrations, bulk crystal-melt and fluid-melt partition coefficients; Supplementary Fig. 1) in a trial-and-error approach to model a single “target” trend that visually matches

the data well, following Humphreys et al. (2021). Although not ideal, the visual match is used because apatite data are typically strongly scattered (as for Laacher See in Humphreys et al., 2021) which makes a numerical fit challenging. To define the target trend, we first need to know the direction of the trend. The data are quite scattered, with no evidence for any strong break in slope that could indicate the onset of volatile saturation (cf. Humphreys et al., 2021) and, although the datasets contain both inclusions and interstitial apatites (Fig. 1), with the latter inferred to crystallise later, their compositions overlap and lack systematic differences in trace element composition (Chelle-Michou and Chiaradia, 2017; Supplementary Fig. 2). There is therefore no firm indication of the direction of the trends, so we attempted to fit each dataset in both directions. We will use the terms ‘upward’ and ‘downward’ based on whether the apatite trend evolves towards higher  $X_{Cl}/X_{OH}$  or lower  $X_{Cl}/X_{OH}$ .

Because the halogens and OH are competing for space in the volatile site in apatite, any individual apatite composition can be reproduced using different sets of initial conditions (initial melt volatile composition, i.e. Cl, F and  $H_2O$  concentrations, bulk crystal-melt and fluid-melt partition coefficients). For instance, a fluorapatite crystal can crystallise from a F-rich melt, or from a melt that has a normal concentration of F but is depleted in OH and Cl. Therefore, having defined our best fit target curve, we use the sensitivity analysis described in Humphreys et al. (2021) to explore this non-uniqueness. Specifically, we use the multistart global optimisation solver, implemented in MATLAB, to explore other combinations of parameters (initial melt volatile composition, i.e. Cl, F and  $H_2O$  concentrations, bulk crystal-melt and fluid-melt partition coefficients, and the  $H_2O$  concentration at fluid saturation) that might also produce close matches to the defined target trend. For each dataset, we run the multistart analysis twice using 800 random seeds each time, first with broad parameter bounds to evaluate the gross effect of wide variations in parameter values, and then with narrower bounds to attempt to define the values that most closely match the target curve, within a narrower range of conditions (Supplementary Data). Each seed is minimized to the target trend to elucidate local minima, where the best fit approximates a global minimum.

#### 4. Model results

Overall, apatite crystals from each unit at Corocochuayco record a

range of compositions that appear to evolve towards lower  $X_{Cl}/X_{OH}$  and higher  $X_F/X_{OH}$  and  $X_F/X_{Cl}$  with evolving whole rock composition (Fig. 1). The gabbrodiorites have distinctively Cl-rich apatite compositions compared to the younger porphyries and rhyodacitic dykes. For each geological unit, we describe below the apatite population compositions, the preferred target trend, and the parameters used to define it. We then discuss the results of a sensitivity analysis that allows us to describe a range of parameters that could also give an acceptable fit to the dataset.

##### 4.1. Gabbrodiorites

The gabbrodiorite apatite compositions for the sample with the largest number of apatite data (10CC09;  $n = 42$ ) vary between  $X_{Cl}/X_{OH} \sim 0.2$ –1.4,  $X_F/X_{OH} \sim 0.5$ –1, and  $X_F/X_{Cl} \sim 0.8$ –2.2 (Figs. 1 and 2). We attempted to model the observed trend both upward and downward (see section 2 in Supplementary). The direction of the trend reflects the changing molar ratios of OH and halogens into apatite with fractionation, as controlled by crystal-melt and fluid-melt partition coefficients and  $K_D$ s (Supplementary Fig. 1). Both trends are visually very similar, with slight deviations in the gradient at the beginning and end of the curve (Supplementary Fig. 3a). Compared to the upward target trend (see Supplementary Table and Supplementary Fig. 3a for more details), the downward target trend required a higher initial melt Cl content (0.35 wt% versus 0.20 wt%), higher  $D_{H_2O}^{xl-m}$  (i.e.  $D_{H_2O}^{xl-m} \sim 0.12$  versus 0.01), lower  $D_{Cl}^{xl-m}$  and  $D_F^{xl-m}$  (i.e.  $\sim 0.20$  versus 0.25 and 0.30 versus 0.40 respectively) and significantly higher fluid-melt partition coefficients (i.e.  $D_{Cl}^{fl-m} \sim 25$  versus 2 and  $D_F^{fl-m} \sim 12$  versus 8). For both trends, we used 5 wt%  $H_2O$  as the saturation level (equivalent to approximately 150 MPa storage pressure in the absence of  $CO_2$  and consistent with previous work). There is no clear evidence in the dataset to suggest that the magma was water-undersaturated when apatite started to crystallise; increasing the saturation pressure (while keeping the magma  $H_2O$ -saturated) would require higher initial melt halogen contents than quoted above. At the proposed crystallisation temperature of 850 °C (Chelle-Michou and Chiaradia, 2017), Tattitch et al. (2021) report  $D_{Cl}^{fl-m} \sim 10$ –25 for intermediate melts at 200 MPa, i.e. similar to the value of the downward target trend. Besides, the values of  $D_F^{fl-m}$  and  $D_{H_2O}^{xl-m}$  required for the upward target trend would be too high and too low, respectively, considering a fractionating

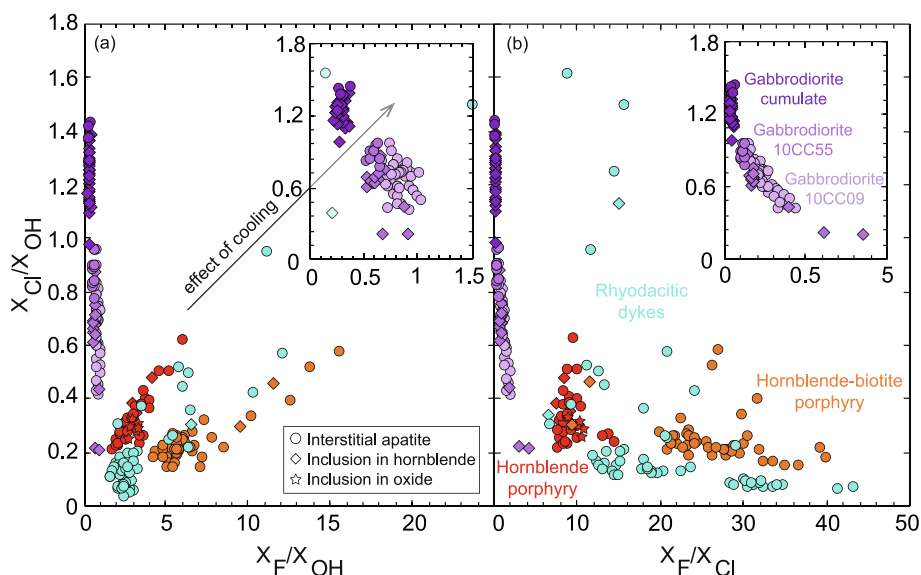


**Fig. 1.** Binary mole ratios ( $X_{Cl}/X_{OH}$  vs  $X_F/X_{OH}$ ) of apatite volatile compositions of the (a) Corocochuayco magmatic suite analysed by EPMA (Supplementary Material 1 of Chelle-Michou and Chiaradia, 2017) and (b) the gabbrodiorite complex only. Note the effect of cooling recorded by high  $X_{Cl}/X_{OH}$  in the rhyodacitic dykes. Ap and hbl stand for apatite and hornblende, respectively. Note the relative errors are 1.9% for F and 5.6% for Cl based on repeated analyses of the Durango (Supplementary Material of Chelle-Michou and Chiaradia, 2017).

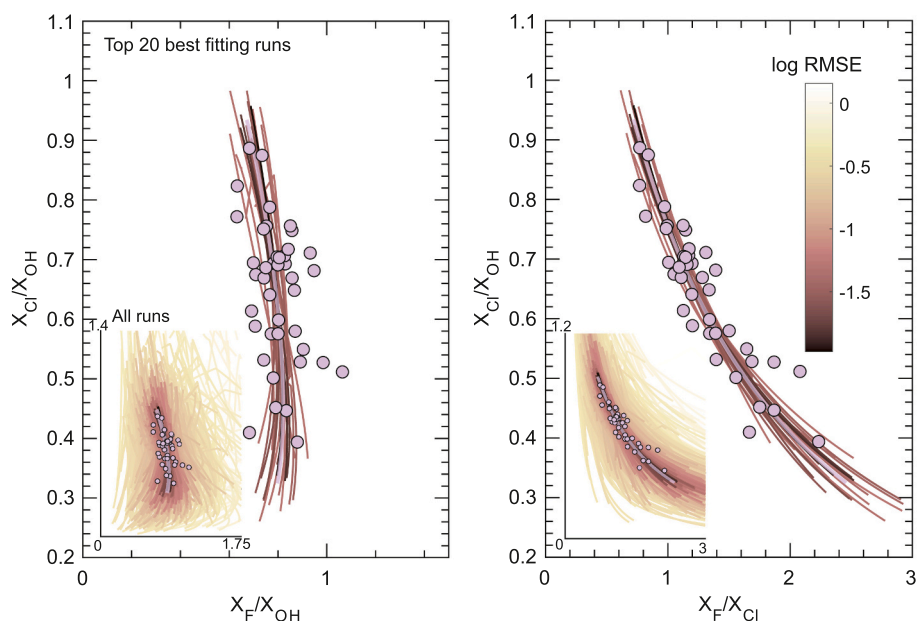


**Fig. 2.** Apatite mole ratios ( $X_{Cl}/X_{OH}$  vs  $X_F/X_{OH}$  and  $X_{Cl}/X_{OH}$  vs  $X_F/X_{Cl}$ ) for the gabbrodiorite with the preferred target trend (thick purple line) and the top 20 successful runs from the results of the `multistart` sensitivity analysis. Note that the `multistart` results are coloured by the logarithm of root mean square error relative to the target trend. Inset plots show the data in the context of all multistart runs. (For interpretation of the references to colour in this figure legend, the reader is referred to the web version of this article.)

assemblage containing amphibole and apatite (Chelle-Michou et al., 2015a, 2015b; Chelle-Michou and Chiaradia, 2017). Thus, we interpret the downward trend as the more geologically reasonable. This was obtained using a water-saturated melt that initially contains 0.35 wt% Cl, 350 ppm F and 5 wt% H<sub>2</sub>O (Table 1).

#### 4.2. Hornblende porphyry

The hornblende porphyry apatite compositions ( $n = 39$ ) vary between  $X_{Cl}/X_{OH} \sim 0.2$ – $0.6$ ,  $X_F/X_{OH} \sim 1.5$ – $6$  and  $X_F/X_{Cl} \sim 7$ – $15$  (Figs. 1 and 3).

The best-fitting upward trend is slightly straighter when plotting  $X_{Cl}/X_{OH}$  vs  $X_F/X_{OH}$  with slopes less steep for  $X_{Cl}/X_{OH}$  vs  $X_F/X_{Cl}$  (Supplementary Fig. 3b) and provides a visually less good fit to the dataset, compared to the downward trend. For both trends, we used 5 wt% H<sub>2</sub>O as the saturation level (equivalent to approximately 150 MPa storage depth in the absence of CO<sub>2</sub>). Compared to the best-fitting upward model (see Supplementary Table 1 for more details), the downward target trend has significantly higher and more reasonable  $D_{Cl}^{xl-m}$  and  $D_F^{xl-m}$  for the fractionating mineral assemblage of hbl + feldspar + magnetite + apatite (i.e.  $D_{Cl}^{xl-m} \sim 0.15$  versus 0.02 and  $D_F^{xl-m} \sim 0.20$  versus 0.07). Compared with the downward

**Table 1**

Estimated Cl melt calculations, initial melt compositions and parameters of the target trend, the mean and standard deviation of the top 20 best fitting runs (i.e., with the 20 lowest RMSEs) and the calculated aggregated fluid compositions following the equations of Tattitch et al. (2021).

Unit by Chelle-Michou and Chiaradia (2017)		Gabbrodiorite	Hbl porphyry	Hbl-bi porphyry	Rhyodacite
Sample		10CC09	10CC64	11CC54	11CC17
Calculated melt chlorine (wt%)					
from apatite <sup>a</sup>		0.6	0.3	0.2	0.16
from amphibole <sup>b</sup>		0.4	0.1	0.1	
Melt fraction at fluid saturation		1	1	0.9	1
	Cl (wt%)	0.35	0.39	0.25	0.45
	F (ppm)	350	1400	1700	1300
Initial melt concentrations	H <sub>2</sub> O (wt%)	5.0	5.0	4.6	5.0
H <sub>2</sub> O saturation level	H <sub>2</sub> O (wt%)	5.0	5.0	5.0	5.0
	Cl	0.20	0.15	0.30	0.15
	F	0.30	0.20	0.40	0.25
Bulk crystal-melt partition coefficients	H <sub>2</sub> O	0.12	0.05	0.01	0.05
	Cl	25	18	17	20
Bulk fluid-melt partition coefficients	F	12	15	9	9
Top 20 mean and std. dev					
	$\bar{x}$ (wt%)	0.37	0.44	0.30	0.46
Initial melt Cl	$2\sigma$	0.04	0.06	0.06	0.08
	$\bar{x}$ (ppm)	380	1600	1930	2330
Initial melt F	$2\sigma$	40	100	20	260
	$\bar{x}$ (wt%)	5.6	6.1	4.4	5.7
Initial melt H <sub>2</sub> O	$2\sigma$	0.8	0.5	0.7	0.9
	Cl (wt% NaCl <sub>eq</sub> )	10.0	8.1	4.3	5.3
Aggregated fluid composition	Cu (ppm)	421	305	284	108

<sup>a</sup> Estimation from apatite (median) by Chelle-Michou and Chiaradia (2017) using the thermodynamic apatite/melt chlorine partitioning model of Li and Hermann (2017) at 850 °C (for gabbrodiorite) and 900 °C (for porphyries).

<sup>b</sup> Estimation from amphibole (average) by Chelle-Michou and Chiaradia (2017) using the calibration of Giesting and Filiberto (2014).

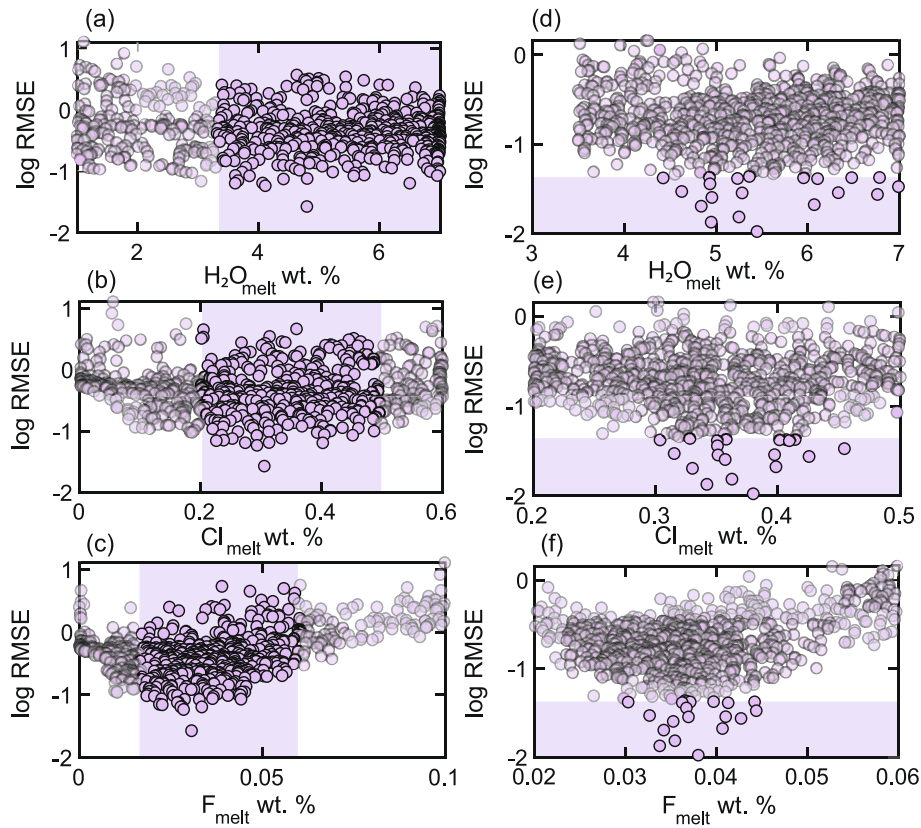


**Fig. 3.** Covariates of the initial melt content in chlorine, fluorine and water (see for the other parameters in the Supplementary) from all successful runs for the gabbrodiorite deposit using broad (a, b, c) and narrow (d, e, f) bounds for the *multistart*. The areas highlighted in purple on the left-hand panels show the parameter ranges used as the narrow bounds. The areas highlighted in purple on the right-hand panels show the range of RMSE for the top 20 best fitting runs (log RMSE ≤ 1.3). The non-transparent runs on the left-hand panels are the runs within the ranges of the narrow bounds whereas the non-transparent runs on the right-hand side are the top 20 best fitting runs. (For interpretation of the references to colour in this figure legend, the reader is referred to the web version of this article.)

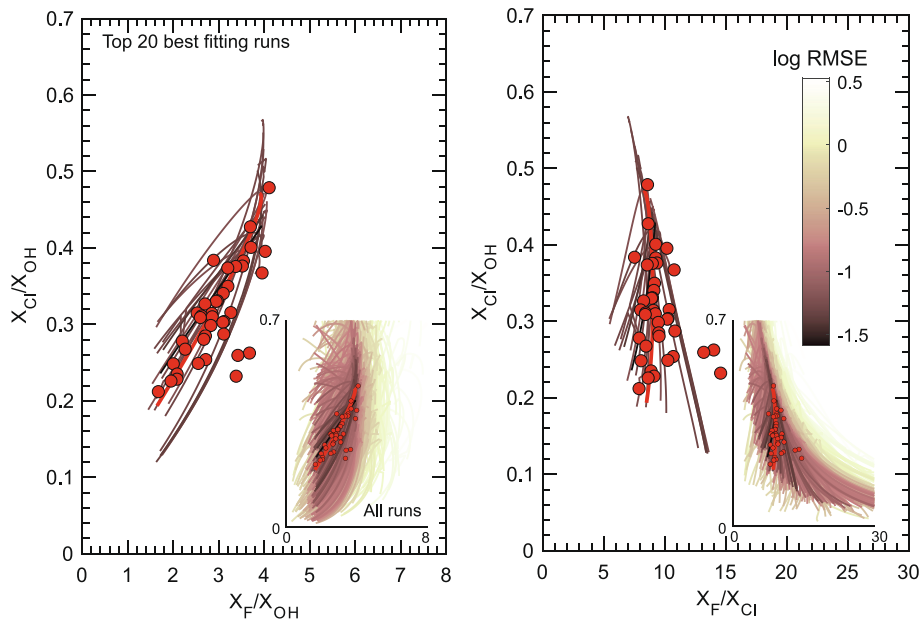


**Fig. 4.** Mole ratios ( $X_{Cl}/X_{OH}$  vs  $X_F/X_{OH}$  and  $X_{Cl}/X_{OH}$  vs  $X_F/X_{Cl}$ ) with the preferred target trend (thick red line) and the top 20 successful runs from the results of the *multistart* sensitivity analysis for the hornblende porphyry. Note that the *multistart* results are coloured by the logarithm of root mean square error relative to the target trend. Inset plots show the data in the context of all *multistart* runs. (For interpretation of the references to colour in this figure legend, the reader is referred to the web version of this article.)

target trend, the fluid-melt partition coefficients for the upward target trend required are lower (i.e.  $D_{\text{Cl}}^{\text{fl-m}} \sim 3$  versus 18 and 3 versus 15, respectively). Hence, due to a qualitatively better fit and more geologically realistic conditions, the preferred model trend is the downward one which is achieved using a water-saturated melt with initial melt compositions of 0.39 wt% Cl, 1400 ppm F and 5 wt%  $\text{H}_2\text{O}$  (Table 1).

#### 4.3. Hornblende-biotite porphyry

The hornblende-biotite (hbl-bi) porphyry apatite compositions ( $n = 35$ ) are quite scattered and vary between  $X_{\text{Cl}}/X_{\text{OH}} \sim 0.14\text{--}0.6$ ,  $X_{\text{F}}/X_{\text{OH}} \sim 4\text{--}7$  and  $X_{\text{F}}/X_{\text{Cl}} \sim 19\text{--}51$  (Figs. 1 and 4). The upward and downward trends are visually very similar (Supplementary Fig. 3c). Compared to the downward target trend (see Supplementary Table 1 for more details), the upward target trend was more challenging to model. It required lower initial melt Cl and F (0.12 wt% Cl versus 0.25 wt% Cl, 1500 ppm F versus 1700 ppm F), and significantly lower fluid-melt partition coefficients (i.e.  $D_{\text{Cl}}^{\text{fl-m}} \sim 2$  versus 17 and  $D_{\text{F}}^{\text{fl-m}} \sim 5$  versus 9). The initial water concentrations were undersaturated relative to 5 wt%  $\text{H}_2\text{O}_{\text{sat}}$  (i.e., 4.6 wt%). There is little to discriminate the two trends, but as with the gabbrodiorites and the hornblende-porphyry, we find the range of  $D_{\text{Cl}}^{\text{fl-m}}$  for such composition/temperature more reasonable for the best-fitting downward model. Additionally, the general trend towards lower  $X_{\text{Cl}}/X_{\text{OH}}$  across the whole dataset suggests the downward trend as the more geologically reasonable. The preferred model trend was obtained using initial melt compositions of 0.25 wt% Cl, 1700 ppm F and 4.6 wt%  $\text{H}_2\text{O}$  at slightly under-saturated conditions (Table 1).

#### 4.4. Rhyodacitic dykes

Neglecting analyses with  $X_{\text{Cl}}/X_{\text{OH}} > 0.9$ , which we interpret are likely to be related to re-equilibration during cooling, following Stock et al. (2018), the rhyodacitic dyke apatite compositions ( $n = 53$ ) are quite scattered and vary between  $X_{\text{Cl}}/X_{\text{OH}} \sim 0.025\text{--}0.6$ ,  $X_{\text{F}}/X_{\text{OH}} \sim 2\text{--}6.5$  and  $X_{\text{F}}/X_{\text{Cl}} \sim 10\text{--}70$  (Figs. 1 and 5). Neither trend fits the data as well as the other units due to the significant scatter of the data. Visually (Supplementary Fig. 3d), the upward target trend provides the best fit when plotting  $X_{\text{Cl}}/X_{\text{OH}}$  versus  $X_{\text{F}}/X_{\text{OH}}$  but the better fit in the plot of  $X_{\text{Cl}}/X_{\text{OH}}$  versus  $X_{\text{F}}/X_{\text{Cl}}$  is given by the downward target trend. Both models were run using the same  $\text{H}_2\text{O}_{\text{sat}}$  (5 wt%). Compared to the downward model (see Supplementary Table 1 for more details), the upward model requires significantly lower melt Cl and F contents (i.e. Cl  $\sim 0.09$  wt% versus 0.45 wt% and F  $\sim 900$  ppm versus 1300 ppm), unreasonably higher F and higher  $\text{H}_2\text{O}$  bulk crystal-melt partition coefficients (i.e.  $D_{\text{F}}^{\text{fl-m}} \sim 0.50$  versus 0.25 and  $D_{\text{H}_2\text{O}}^{\text{fl-m}} \sim 0.20$  versus 0.05), as well as notably lower fluid-melt partition coefficients for Cl and F (i.e.  $D_{\text{Cl}}^{\text{fl-m}} \sim 1$  versus 20 and  $D_{\text{F}}^{\text{fl-m}} \sim 2$  versus 9). This means that the fluid-melt partition coefficient of Cl is smaller than that of F for the upward target trend, unrealistic with the more compatible behaviour of Cl in the fluid compared to F. Although the downward target trend does not fit the scattered data with  $X_{\text{Cl}}/X_{\text{OH}} > 0.4$ , it results in a better fit for the tail with high  $X_{\text{F}}/X_{\text{Cl}}$  (i.e.  $X_{\text{F}}/X_{\text{Cl}} > 30$ ) and seems geologically more realistic than the upward target trend. We attempted to model a target trend that would fit the apatites with high  $X_{\text{Cl}}/X_{\text{OH}}$  better; this resulted in a steeper and better-fitting trend for  $X_{\text{F}}/X_{\text{Cl}}$  versus  $X_{\text{F}}/X_{\text{Cl}}$ , but performed poorly for the high  $X_{\text{F}}/X_{\text{Cl}}$  tail. However, this model requires unreasonably higher bulk crystal-melt partition coefficient for rhyodacitic compositions ( $D_{\text{F}}^{\text{fl-m}} \sim 0.5$ ) and higher fluid-melt partition

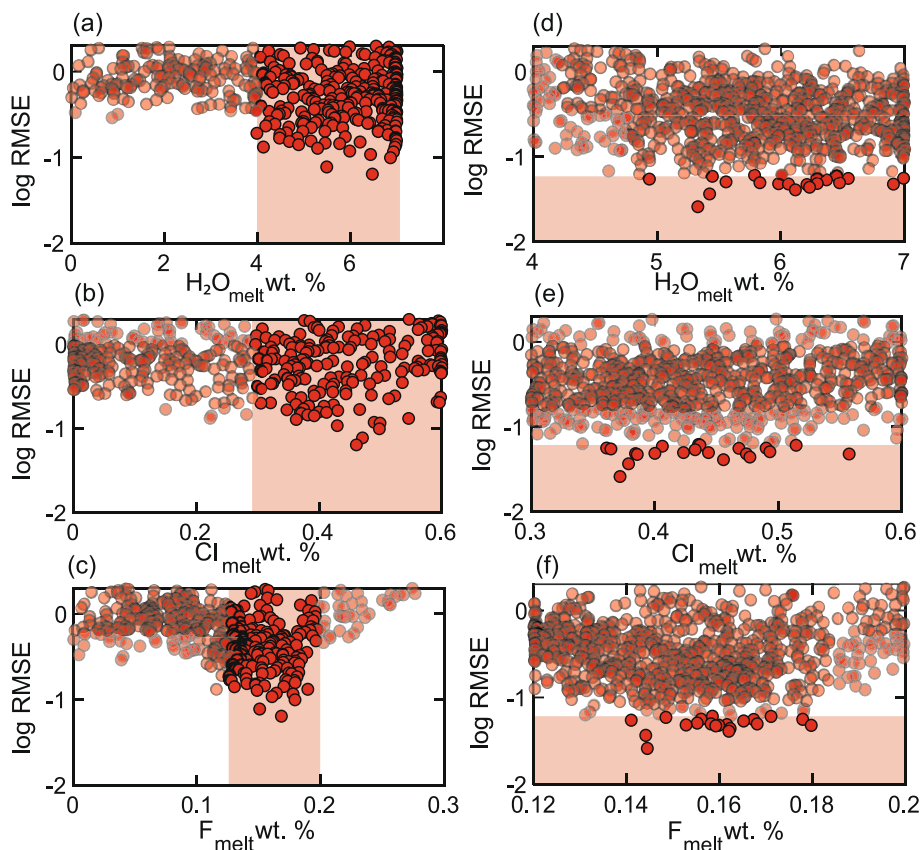


**Fig. 5.** Covariates of the initial melt content in chlorine, fluorine and water from all successful runs for the hornblende porphyry deposit using broad (a, b, c) and narrow (d, e, f) bounds for the `multistart`. The areas highlighted in red on the left-hand panels show the parameter ranges used as the narrow bounds. The areas highlighted in red on the right-hand panels show the range of RMSE for the top 20 best fitting runs ( $\log \text{RMSE} \leq 1.2$ ). The non-transparent runs on the left-hand panels are the runs within the ranges of the narrow bounds whereas the non-transparent runs on the right-hand side are the top 20 best fitting runs. (For interpretation of the references to colour in this figure legend, the reader is referred to the web version of this article.)

coefficient ( $D_F^{\text{fl-m}} \sim 15$ ). Hence, the preferred model trend is achieved using a water-saturated melt with initial melt compositions of 0.45 wt% Cl, 1300 ppm F and 5 wt%  $H_2O$ , bulk crystal-melt partition coefficients are 0.15 for Cl, 0.25 for F and 0.05 for  $H_2O$  and the fluid-melt partition coefficients are 20 for Cl and 9 for F (Table 1).

#### 4.5. Multistart outputs

We have established, above, the reasons why we prefer the downward model trends (target curves) for each unit. We then performed a sensitivity analysis for these trends using the multistart global minimization algorithm (Dixon and Szegő, 1978; Glover, 1998; Zsolt et al., 2007) within the code of Humphreys et al. (2021), which we updated to include the water saturation level,  $H_2O_{\text{sat}}$ , as a variable and to exclude the apatite-melt  $K_D$ s, which are now tied to temperature and apatite composition as described above. Here, we show the results of the sensitivity analysis as lines coloured by RMSE (root mean square error i. e. goodness of fit to the target trend) in the binary mole fraction ratio figures, and as covariate plots of parameter value against RMSE (Figs. 2–9). The multistart outputs are also reported in Table 1 and in the Supplementary information.

For each unit, we ran two iterations of the sensitivity analysis, where initial seeds are randomly chosen using first broad and then narrow bounds for the input parameters. The broad bounds are chosen based on the constraints from previous studies (e.g. Chelle-Michou and Chiaradia, 2017) and from the existing experimental values found in the literature, especially for the partition coefficients. The results from the multistart runs with broader bounds allows us to target the narrower parameter bounds used next, based on the values yielding low RMSE. For example, the results from the broader bounds runs for the gabbrodiorite clearly point to lower RMSE at  $F < \sim 0.05$  wt% (Fig. 3c).

For the gabbrodiorites (Figs. 2, 3 and Supplementary Fig. 4.1), the 20 best fitting runs are scattered on either side of the preferred model fit. Initial melt compositions, based on the initial parameter values used for these best-fitting successful runs, are likely in the range 4.6–6.6 wt%  $H_2O$ , 0.3–0.45 wt% Cl and 0.03–0.045 wt% F. There is no appreciable variation of other parameters with RMSE (Supplementary Fig. 4.1). Multistart minima with higher RMSE start with initially higher  $X_{\text{Cl}}/X_{\text{OH}}$  and tend towards higher  $X_{\text{F}}/X_{\text{OH}}$ ; these runs tend to have lower initial

melt Cl and higher melt F contents with lower initial  $H_2O$  (Fig. 3).

For the hbl porphyry, only a few of the best fitting runs are a good visual fit to the data, with several of the top 20 model results lying outside the main dataset (Fig. 4). This suggests that there is a relatively tightly defined set of parameter combinations that also match the target trend, such that only a few of the 800 random seeds, within our chosen parameter bounds (Supplementary Fig. 4.2a), return good matches to the target trend. Inspection of the model data suggests that the best fitting minima, i.e., those with lowest log(RMSE), have initial melt  $H_2O$  ( $> 5$  wt%),  $H_2O_{\text{sat}}$  ( $> 5$  wt%), intermediate initial melt Cl ( $\sim 0.4$ – $0.5$  wt%), and moderate initial melt F contents (0.14–0.18 wt% F, Fig. 5), as well as moderate  $D_{\text{xl-m}}^{H_2O}$  ( $\sim 0.1$ – $0.3$ ; see Supplementary Fig. 4.2).

The hbl-bi porphyry modelling returns a spread of runs somewhat symmetrically distributed around the preferred model fit (Fig. 6). The top 20 best fits are all within the broad spread of the dataset, but many minima with  $\log \text{RMSE} \geq -1$  are clearly not visually acceptable (Figs. 6 and 7). As with the hbl porphyry, the best fitting minima have initial melt  $H_2O$  concentrations of 4–6 wt%, moderate fluorine contents (0.15–0.23 wt%) and 0.2–0.4 wt% Cl (Fig. 7). There is no clear variation of RMSE with bulk crystal-melt partition coefficients or with  $D_{\text{fl-m}}^{\text{Cl}}$ , but we see a strong tendency for the best fitting model results to have high  $D_{\text{fl-m}}^{\text{F}}$  ( $> 7$ ) (see Supplementary Fig. 4.3b).

The rhyodacite porphyry is more challenging to assess because of the scatter in the dataset (Fig. 8), but the minima closest to the preferred model fit have high initial melt  $H_2O$  (4–7 wt%) and Cl (0.3–0.6 wt%) and intermediate initial melt F (0.18–0.28 wt%) (Fig. 9). Runs with the lowest log(RMSE) also have lower  $D_{\text{xl-m}}^{H_2O}$  and higher  $D_{\text{xl-m}}^{\text{F}}$  (Supplementary Fig. 4.4a-b) and higher  $H_2O_{\text{sat}}$  ( $> 5$  wt%; see Supplementary Fig. 4.4a).

Finally, the multistart results show trade-offs between the melt compositions. For instance, there are strong trade-offs between the fluorine melt composition and the melt  $H_2O$  for all the deposits, particularly for the hbl-bi porphyry and the rhyodacite (Supplementary Fig. 5.1). In other words, the best models require either low F and low  $H_2O$  or high F and high  $H_2O$ . The gabbrodiorites also shows trade-offs between Cl and  $H_2O$  (Supplementary Fig. 5.2) in the melt hence the trade-off between Cl and F (Supplementary Fig. 5.3) whereas the other units do not show clear correlation. Regarding the crystal-melt and the fluid-melt partition coefficients, there are no clear trade-offs

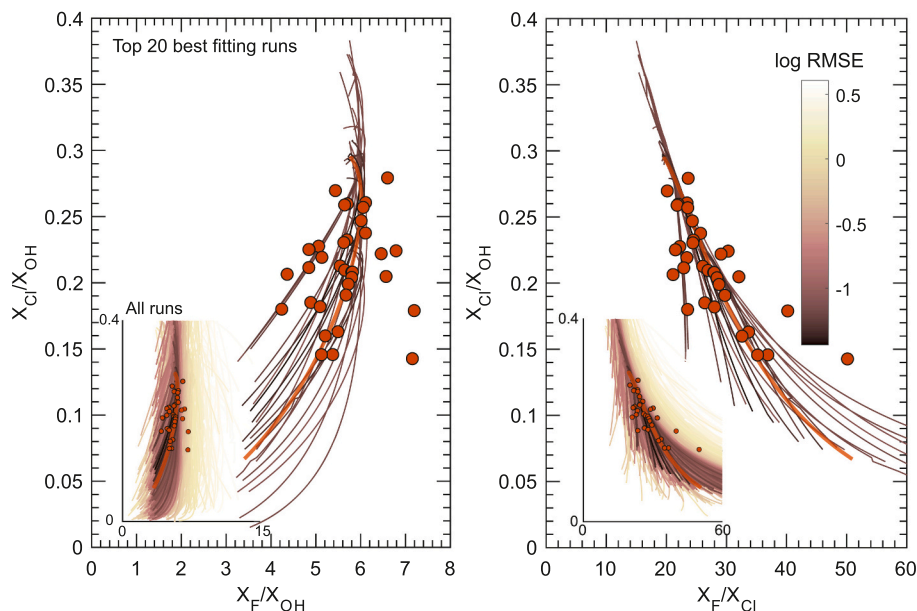


**Fig. 6.** Mole ratios ( $X_{\text{Cl}}/X_{\text{OH}}$  vs  $X_{\text{F}}/X_{\text{OH}}$  and  $X_{\text{Cl}}/X_{\text{OH}}$  vs  $X_{\text{F}}/X_{\text{Cl}}$ ) with the preferred target trend (thick orange line) and the top 20 successful runs from the results of the multistart sensitivity analysis for the hornblende-biotite porphyry. Note that the multistart results are coloured by the logarithm of root mean square error relative to the target trend. Inset plots show the data in the context of all multistart runs.

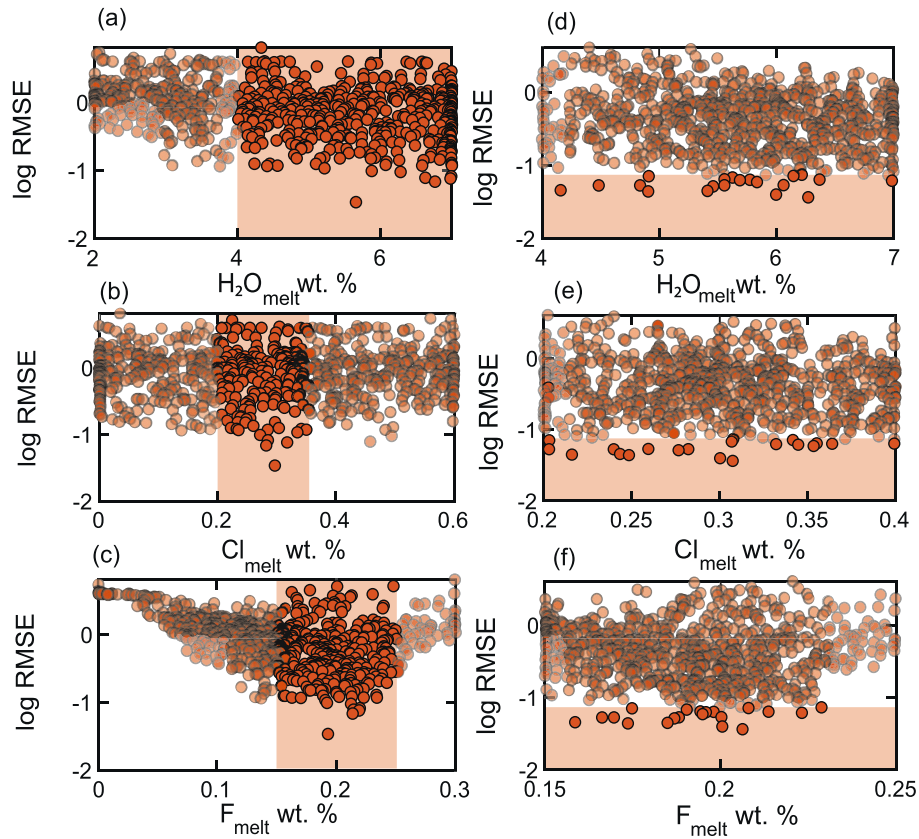


**Fig. 7.** Covariates of the initial melt content in chlorine, fluorine and water from all successful runs for the hornblende-biotite porphyry deposit using broad (a, b, c) and narrow (d, e, f) bounds for the *multistart*. The areas highlighted in orange on the left-hand panels show the parameter ranges used as the narrow bounds. The areas highlighted in orange on the right-hand panels show the range of RMSE for the top 20 best fitting runs ( $\log \text{RMSE} \leq 1.1$ ). The non-transparent runs on the left-hand panels are the runs within the ranges of the narrow bounds whereas the non-transparent runs on the right-hand side are the top 20 best fitting runs.

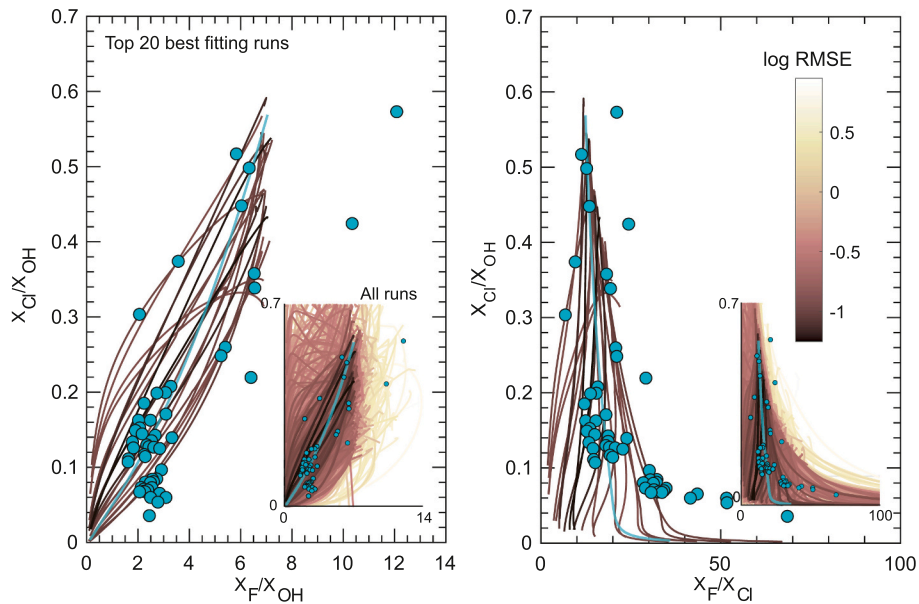


**Fig. 8.** Mole ratios ( $X_{\text{Cl}}/X_{\text{OH}}$  vs  $X_{\text{F}}/X_{\text{OH}}$  and  $X_{\text{Cl}}/X_{\text{OH}}$  vs  $X_{\text{F}}/X_{\text{Cl}}$ ) with the preferred target trend (thick blue line) and the top 20 successful runs from the results of the *multistart* sensitivity analysis for the rhyodacitic dykes. Note that the *multistart* results are coloured by root mean square error relative to the target trend. Inset plots show the data in the context of all *multistart* runs. Note that data points with  $X_{\text{Cl}}/X_{\text{OH}} > 0.8$  were discarded during modelling as they may have undergone re-equilibration during cooling (see text). (For interpretation of the references to colour in this figure legend, the reader is referred to the web version of this article.)

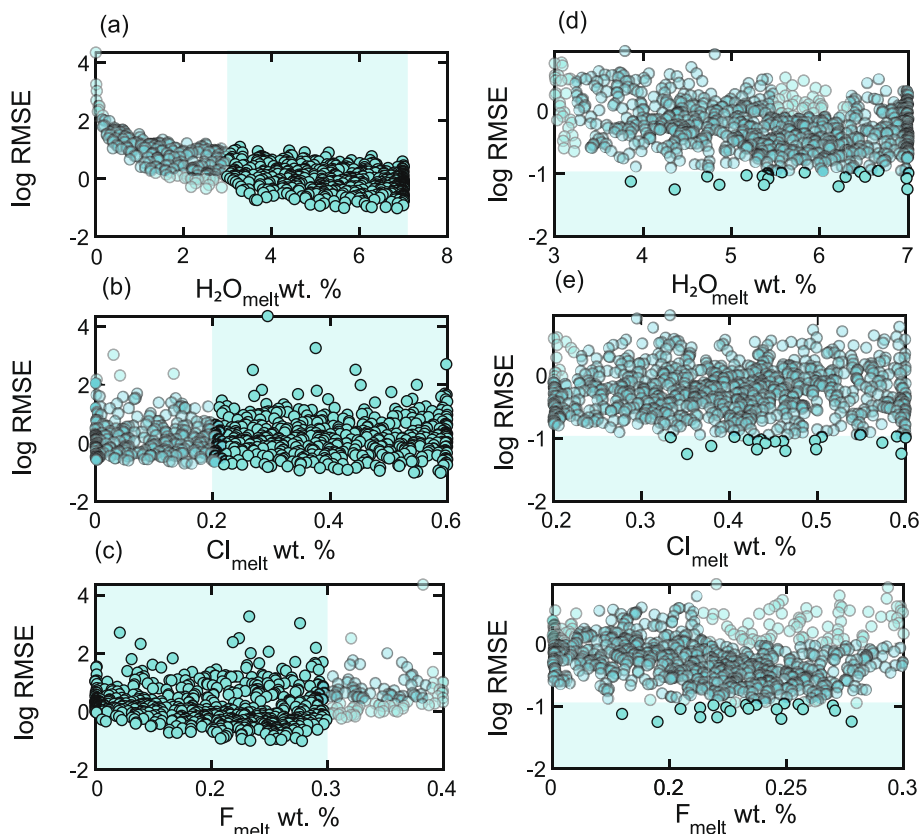


**Fig. 9.** Covariates of the initial melt content in chlorine, fluorine and water from all successful runs for the rhyodacitic dykes using broad (a, b, c) and narrow (d, e, f) bounds for the *multistart*. The blue shading in the left-hand panels shows the parameter ranges used as the narrow bounds. The blue shading on the right-hand panels shows the range of RMSE for the top 20 best fitting runs ( $\log \text{RMSE} \leq 0.96$ ). The non-transparent runs on the left-hand panels are the runs within the ranges of the narrow bounds whereas the non-transparent runs on the right-hand side are the top 20 best fitting runs. (For interpretation of the references to colour in this figure legend, the reader is referred to the web version of this article.)

(Supplementary Fig. 5.4, 5.5) except between the fluid-melt partition coefficients of F and Cl for the hbl porphyry (Supplementary Fig. 5.5).

## 5. Discussion

In this contribution, we have improved the model of Humphreys et al. (2021) by including the non-ideal mixing of the volatile species in apatite solid solution and temperature-dependence of  $K_{\text{DS}}$  defined by Li and Costa (2020, 2023) at each increment of bulk crystal fractionation. We have also included the H<sub>2</sub>O saturation point as a variable within the sensitivity analysis. A bespoke temperature-crystallinity curve can also be used in place of a fixed temperature if desired. This allows us to track the volatile evolution of the Corocochuayco magmatic suite before, during and after the mineralisation of a magmatic system (Fig. 10). Nevertheless, a limitation of the model remains that the bulk partition coefficients are assumed constant with fractionation, whereas  $D_i^{\text{fl-m}}$  and  $D_i^{\text{xl-m}}$  may, in principle, vary during differentiation. However, given the degree of scatter in the apatite data – which could be related to any combination of analytical uncertainty, local variations in temperature or composition, or minor post-crystallisation modification – relative to the trajectory of the model, we cannot resolve any such variations and conclude that there is no evidence that the bulk partition coefficients varied substantially during crystal-melt fractionation and fluid exsolution.

### 5.1. Timing of apatite crystallisation and the potential for re-equilibration

The gabbrodiorites dataset considered in this study (i.e., unit 10CC09, Fig. 1) only includes late-stage interstitial apatite grains found

between plagioclase primocrysts (Chelle-Michou and Chiaradia, 2017). Interstitial apatites have the potential to re-equilibrate during cooling or late-stage fluid flow by exchanging halogens with their surroundings, whereas inclusions within solid phases are unlikely to do this effectively (Bernard et al., 2022; Stock et al., 2018). However, the late-stage interstitial apatite grains considered here overlap in composition with apatite inclusions found in the 10CC55 gabbrodiorite unit (Fig. 1). This implies that re-equilibration in the late-stage interstitial apatite grains was minor. On the contrary, the datasets of the porphyries and the rhyodacite include both interstitial apatite grains and mineral-hosted inclusions of apatite (Fig. 1) which overlap on Fig. 1. For each unit of the porphyries, the similarity of chemistry between the apatites found in the groundmass and as inclusions suggests relatively early apatite saturation (Chelle-Michou and Chiaradia, 2017) and negligible re-equilibration of the groundmass apatites. Some rhyodacite apatites with anomalously high Cl and F ( $X_{\text{Cl}}/X_{\text{OH}} > 0.8$  and  $X_{\text{F}}/X_{\text{OH}} > 15$ , Fig. 1a) and elevated S, Mg and Na compared to the rest of the dataset (Supplementary data of Chelle-Michou and Chiaradia, 2017) possibly indicate that they could have been affected by late-stage processes such as cooling (Stock et al., 2018) or by interaction with fluids. Based on the distinct chemistry as well as their low abundance, we treated these as outliers and excluded them from the modelling as the model does not account for late-stage processes.

### 5.2. Water saturation and melt volatile composition

The target trends and *multistart* modelling show that in all units the melt needs to be volatile-saturated (or very close to volatile saturation) to fit the trends in apatite composition. The *multistart* modelling results

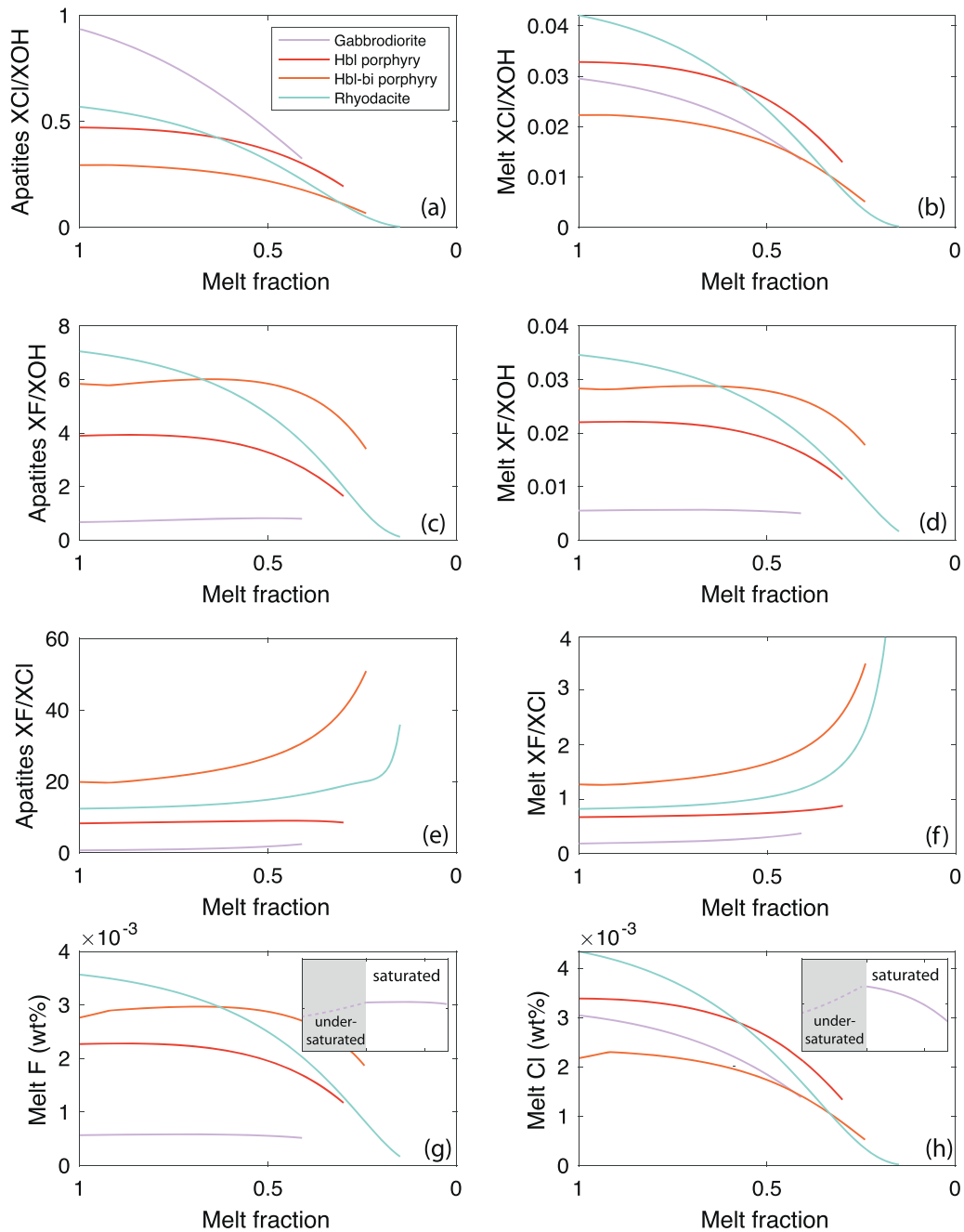


**Fig. 10.** Volatile evolution in apatite (a, c, e) and melt (b, d, f, g, h) during apatite crystallisation of the Corocochuayco magmatic suite. Note that the original gabbrodiorite melt i.e., prior to apatite crystallisation, was volatile-undersaturated with lower volatile contents (see text for more details). For reference, the pre-apatite evolution of the gabbrodiorites is represented as inserts in panels (g) and (h) as a dashed line.

(Figs. 2–9) show that the top 20 best fitting runs are volatile saturated or reach volatile saturation after an average of 6% crystallisation for the gabbrodiorites, 5% for the hbl porphyry, 8% for the hornblende-biotite porphyry, and 4% for the rhyodacite. When volatile saturation is reached, chlorine is extracted into the exsolving fluid according to its  $D_{fl-m}^{Cl}$  (Table 1), and this is commonly seen as a decrease of  $X_{Cl}/X_{OH}$  in apatite (Figs. 2, 4, 6, and 10), although this also depends on other parameters chosen, as discussed above (Candela, 1986; Humphreys et al., 2021; Stock et al., 2016). To illustrate this point, after 50% crystal-melt fractionation, our models indicate that the initial gabbrodiorite melt has lost approximately 40% of the Cl that it held at volatile saturation, while the hbl porphyry, the hbl-bi porphyry and the rhyodacite melts have lost ~23%, 20%, and 29% of their Cl content, respectively (cf.

Supplementary information). In contrast, because  $D_{fl-m}^{Cl} > D_{fl-m}^F > 1$ , fluorine may initially keep increasing in the evolving melt despite also being extracted into the fluid upon saturation (Humphreys et al., 2021). After the same 50% crystal-melt fractionation (but starting from the saturation of apatite), according to our models the residual melt in the gabbrodiorites was only 2% depleted in fluorine relative to its concentration at volatile saturation, the hbl porphyry had 14% lower fluorine, the hbl-bi-porphyry and the rhyodacite melt were slightly elevated in fluorine relative to their initial levels at volatile saturation. Therefore, we infer that most of the melts had exsolved a relatively small fraction of their total volatile budget (cf. Nathwani et al., 2023).

When a melt that is initially water-undersaturated then becomes water-saturated, the modelled apatite trend shows a sharp or

progressive change in slope (Supplementary Fig. 3). None of the datasets shows a clear break in slope that can clearly demonstrate the onset of water saturation. However, within the scatter of the data, we cannot exclude a short period of initially volatile-undersaturated crystallisation, and this is reflected in the multistart modelling results, for which the initial melt H<sub>2</sub>O concentration of the best fits is typically at, or just below, the H<sub>2</sub>O saturation level used in the model. This could relate to the sweet spot described by Brookfield et al. (2023) who found that the highest overpressure of volcanic systems is reached when the magma is at its water solubility limit.

Overall, the inferred initial melt volatile contents based on apatite geochemistry are very similar for the individual units (Table 1). However, it is important to note that this is the melt volatile content when apatite saturates. A major distinction is that apatite in the gabbrodiorites is relatively late crystallising (forms inclusions in interstitial amphibole and fills other interstitial spaces) whereas apatite in the other units crystallises early, alongside other major phases (Chelle-Michou and Chiaradia, 2017). Therefore, apatites in the gabbrodiorite unit crystallised from a more evolved interstitial melt (andesitic) that had previously fractionated an assemblage dominated by plagioclase (Chelle-Michou et al., 2015a, 2015b). The original gabbrodiorite parental melt would therefore have been volatile-undersaturated with significantly lower initial volatile contents (cf. inserts in panels g and h from Fig. 10); assuming 40% prior fractionation (Chelle-Michou et al., 2015a, 2015b), application of suitable bulk  $D^{xl-m}$  suggests that the initial gabbrodiorite melt would have had ~0.245 wt% Cl, 3.5 wt% H<sub>2</sub>O and ~240 ppm F. This means that the gabbrodiorite would only reach volatile saturation after around 50% crystal-melt fractionation, when the magma had already reached a mushy state.

### 5.3. Bulk crystal-melt and fluid-melt partition coefficients

The multistart results typically show that the model fit does not depend strongly on the bulk crystal-melt partition coefficients, as there is no variation of RMSE over the (wide) ranges explored (e.g. Supplementary Figs. 4.1a, 4.2a, 4.3a, 4.4a). This is likely because the bulk crystal-melt partition coefficients for Cl and F do not have a significant control on the shape or orientation of the apatite trend, relative to other parameters that dominate (cf. Supplementary Fig. 1). Moreover, bulk crystal-melt partition coefficients for halogens and H<sub>2</sub>O in silicates are very low (<<0.1) except for amphibole, apatite, and biotite. Based on the observed compositions and modal proportions of these phases (Chelle-Michou et al., 2015a, 2015b), realistic bulk crystal-melt partition coefficients would likely not exceed approximately 0.3–0.4 for Cl and F, and ~0.25 for H<sub>2</sub>O. Therefore, the bulk crystal-melt  $D_s$  used for our preferred fits (Table 1) are within reasonable limits. In contrast, the fluid-melt partition coefficients can strongly influence the modelled apatite trend (Supplementary Fig. 1). For all units, we require high  $D_{Cl}^{fl-m}$  (in the range 17–25, Table 1) which indicates strong degassing of Cl into the fluid. These values are consistent with the values derived from experimental data of similar composition, temperature and pressure (i.e. 10–25 at 200 MPa; Tattitch et al., 2021; Dolejš and Zajaczk, 2018; i.e. 3.5–22.7 between 150 and 400 MPa; Iveson et al., 2017). We also require  $D_F^{fl-m}$  values that appear high (i.e.  $D_F^{fl-m} \geq 9$ , Table 1) compared to some values reported in the literature (i.e. typically 0.1–1, Borodulin et al., 2009 but with higher values e.g. 1.5–6 for rhyodacite and 12–31 for basalt, Chevychelov et al., 2008a). However, these values are consistent with elevated values ( $D_F^{fl-m} > 10$ ) determined experimentally in phonolitic magmas (Chevychelov et al., 2008b) and in basaltic melts (Chevychelov et al., 2008a). The modelled fractionation trends suggest that for all units, fluorine initially continues to increase in the melt after volatile saturation, before starting to decrease at a rate that depends on the combination of  $D_F^{xl-m}$  and  $D_F^{fl-m}$ . To have a good fit of the apatite trends with a lower  $D_F^{fl-m}$  (i.e. ~1–2) would typically require a combination of extracting F more quickly from the melt relative to H<sub>2</sub>O via crystal growth (i.e. using a higher bulk  $D_F^{xl-m}$ ) and extracting Cl more

quickly from the melt either using a higher bulk  $D_{Cl}^{xl-m}$  and/or higher  $D_{Cl}^{fl-m}$ . For example, the gabbrodiorites trend could be fitted using  $D_F^{fl-m} = 2$  but this requires unreasonably high  $D_{Cl}^{xl-m}$  (~100),  $D_{Cl}^{fl-m}$  (0.4) and  $D_F^{xl-m}$  (0.8). We also note that the broad-bounds multistart analysis of the hornblende-biotite porphyry and the rhyodacite clearly show that RMSE are lower for higher  $D_F^{fl-m} >> 1$  (see Supplementary Figs. 4.3a and 4.4a).

### 5.4. The role of magmatic halogens in the fertility of ore deposits

Hydrous, Cl-enriched melts are thought to be a key ingredient to increase metal endowment leading to formation of economic metal deposits (Tattitch et al., 2021). In this study, there is no clear difference in the modelled initial melt water and chlorine content (5 wt% H<sub>2</sub>O and 0.25–0.45 wt% Cl) between the pre-mineralisation gabbrodiorites, the later mineralising porphyries and the post-mineralisation rhyodacite), while fluorine is significantly less abundant in the initial melt for the gabbrodiorites (~350 ppm compared with ~1500 ppm). However, considering that the gabbrodiorite apatite only started crystallising when the melt reached andesitic composition (Chelle-Michou et al., 2015a, 2015b, Chelle-Michou and Chiaradia, 2017), this implies that the gabbrodiorite parental melt had lower H<sub>2</sub>O, Cl and F than that forming the porphyries (see also above). However, the melt concentrations inferred here are not anomalously high and are not necessarily responsible for the fertility of the Corocochuayco magmas, consistent with Chelle-Michou and Rottier (2021). The fluorine concentrations seem to be the main distinctive component value between the pre- and syn-mineralising deposits based on the results of our model. We speculate that fluorine may enhance ore fertility by impacting the transport of metals (McPhie et al., 2011) or by increasing the porosity of the host rock and enhancing mineral replacement reactions (Xing et al., 2019), thus improving the leaching of metals and creating fluid pathways. However, as discussed in Chelle-Michou and Rottier (2021), the fertility of ore magmas is probably not due to a special chemistry and may instead, be controlled by physical components such as the volume and magma flux of a system, its lifetime, its thermal gradient and the rheology of the intruded crust and the magma flux.

### 5.5. Fluid salinity and its copper loads

Fluid inclusions are unique and direct windows onto the compositions of the fluids released incrementally during crystallisation and they record the fluid composition at the time of capture. The fluids that transport metals into porphyry copper deposits are equivalent to the aggregation of these instantaneous fluids released during magmatic differentiation (Tattitch et al., 2021). Volatile-bearing minerals such as apatite represent an independent means to model volatile evolution in fluids. Below, we use the results from our apatite modelling to calculate both instantaneous and aggregated fluid salinities during crystallisation of the porphyry-generating magmas, following Tattitch et al. (2021). We thus calculate the instantaneous salinity of the fluid phase at each point in the fractionation sequence from our modelled outputs as:

$$NaCl_{inst} = Cl_m \bullet D_{Cl}^{fl-m} \bullet \frac{m_{NaCl}}{m_{Cl}} \quad (3)$$

where  $m$  is molar mass and all Cl<sup>-</sup> are assumed to be complexed with Na<sup>+</sup> (Chelle-Michou and Chiaradia, 2017). Then, we calculate the aggregated fluid, following Eqs. (15) and (16) of Tattitch et al. (2021):

$$NaCl_{aggr,fl} = \frac{1}{m_{fluid_n}} \sum_{i=1}^n NaCl_{fluid_i} \bullet (m_{fluid_i} - m_{fluid_{i-1}}) \quad (4)$$

where,

$$m_{fluid_i} = m_{water_i} + (m_{water_i} - m_{water_{i-1}}) \bullet \frac{NaCl_{fluid_i}}{100 - NaCl_{fluid_i}} \quad (5)$$

We also calculated the instantaneous and aggregated Cu fluid

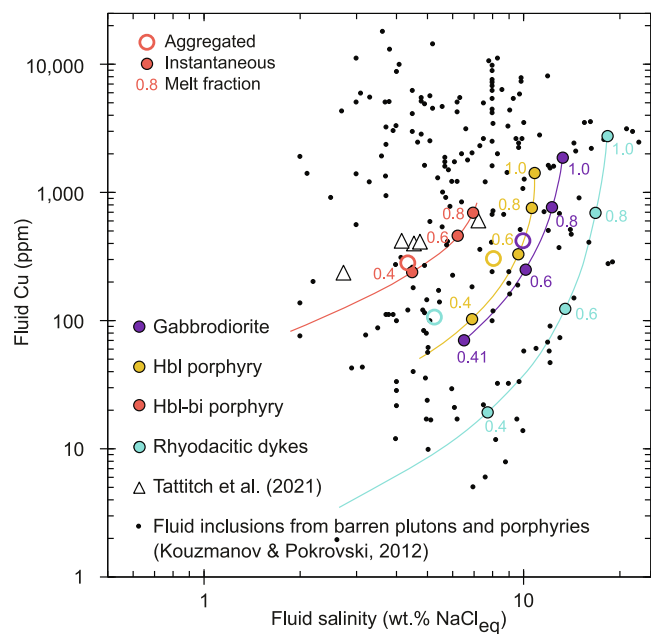


**Fig. 11.** Modelled fluid salinity and fluid copper content of the Corocochuayco magmatic suite, after [Tattitch et al. \(2021\)](#) using  $D_{Cu}^{fl-m} = 0.1$ . The gabbrodiorites and the rhyodacitic dykes were emplaced pre- and post-mineralisation but are plotted for reference. The white triangles are the aggregated fluid salinity and Cu inferred from the Monte Carlo simulations of degassing and crystallisation from [Tattitch et al. \(2021\)](#) and the black circles are analysed single-phase fluid inclusions for deep barren plutons, Cu–Au (Mo) porphyries and associated skarn deposits ([Kouzmanov and Pokrovski, 2012](#)). Small, coloured circles are instantaneous salinities at different melt fraction whereas the larger ones are aggregated salinities calculated over the whole target trend for each unit. The instantaneous salinities for the gabbrodiorite, the hornblende-porphyry and the rhyodacite follow the same trend of decreasing Cu content and fluid salinity with decreasing melt fraction.

content. We used an initial melt Cu concentration  $\sim 35$  ppm (i.e., average of the range for intermediate arc magmas; [Tattitch and Blundy, 2017](#)), and assumed a constant  $D_{Cu}^{fl-m}$  ( $\sim 0.1$ ), and we computed the salinity of the exsolved fluid to calculate  $D_{Cu}^{fl-m}$  following Eq. (14) of [Tattitch and Blundy \(2017\)](#), for which we ignored the  $H_2S$  component for simplicity. We then replaced NaCl by Cu in Eqs. (3), (4) and (5) to calculate the instantaneous and the aggregated Cu content in the fluid, following [Tattitch et al. \(2021\)](#). Although the gabbrodiorites and the rhyodacitic dykes are pre- and post-mineralising units and did not contribute to the mineralisation of the Corocochuayco system, we report them for reference. We obtain instantaneous fluid salinity ranging from 6.5 to 13.3 wt% NaCl<sub>eq</sub> for the gabbrodiorite, 4.7 to 10.9 wt% NaCl<sub>eq</sub> for the hornblende porphyry, 1.9 to 7.1 wt% NaCl<sub>eq</sub> for the hornblende-biotite porphyry and 0.2 to 18.4 wt% NaCl<sub>eq</sub> for the rhyodacitic dykes (see Supplementary Material), in good agreement with both [Tattitch et al. \(2021\)](#) and [Nathwani et al. \(2023\)](#). However, in contrast to [Nathwani et al. \(2023\)](#) our modelled instantaneous fluids become less saline with fractionation as Cl is progressively extracted from the melt. This is likely because we do not address the variation of  $D_{fl-m}^{Cl}$  with melt SiO<sub>2</sub> content and pressure and instead use constant values for each fractionation model, although we do test a range of values through the sensitivity analysis. We prefer this approach because both melt SiO<sub>2</sub> content and pressure are relatively poorly constrained for our case study, and the variation of SiO<sub>2</sub> with melt fraction in the approach of ([Tattitch et al., 2021](#)) also adds significant uncertainty. The corresponding aggregated salinities for the target trend for each magmatic unit are 10 wt%, 8 wt%, 4 wt% and 5 wt% NaCl<sub>eq</sub>, respectively ([Table 1](#)). We obtain instantaneous Cu fluid ranging from 71 to 1883 ppm for the gabbrodiorite, 50 to 1424 ppm for the hornblende porphyry, 81 to 822

ppm for the hornblende-biotite porphyry and 0.6 to 2746 ppm for the rhyodacitic dykes. The aggregated Cu fluid content is 421 ppm for the gabbrodiorite, 305 ppm for the hornblende porphyry, 284 ppm for the hornblende-biotite porphyry and 107 ppm for the rhyodacitic dykes. These ranges agree well with the range of fluid salinities and fluid Cu content calculated from degassing paths ([Tattitch et al., 2021](#)) and with single-phase fluid inclusions from porphyry deposits and associated skarns ([Fig. 11](#)).

Our data do not indicate systematic differences in fluid salinity between the mineralising and non-mineralising units in this locality. This may mean that other factors not accounted for here, such as dissolved melt sulphur concentrations, are important in determining copper fertility. However, this work shows that apatite can be a good alternative means of reconstructing the evolving magmatic fluid salinity and linking this to its trace metal loads.

## 6. Conclusions

A crystal  $\pm$  fluid fractionation model is applied to interpret crystallisation conditions for apatite-bearing magmas from the Corocochuayco Fe-Cu-Au porphyry-skarn deposit. Using the apatite dataset of [Chelle-Michou and Chiaradia \(2017\)](#), we apply and further develop this model for the first time to porphyry-forming magmas. The model includes the T-dependent exchange coefficients  $K_D$ s defined by [Li and Costa \(2020, 2023\)](#) to factor the non-ideal mixing of OH-F-Cl in apatite. Our apatite model highlights the importance of determining the direction of the apatite trend in the mole ratio space (i.e. whether the evolution tends towards higher or lower Cl/OH or F/OH, either defined by textural constraints or by apatite trace element chemistry). Additionally, we show that the fluid-melt partition coefficients govern the evolution of the apatite trend for fluid-saturated magmas, and may be a good discriminatory tool in picking the best model. Our best-fitting models require melts that are volatile-saturated (or very nearly so) at the time of apatite saturation. However, the pre-mineralising gabbrodiorite had a substantial prior phase of volatile-undersaturated crystallisation suggesting that its original magma would have been initially volatile-undersaturated as well as apatite-undersaturated. There is no significant difference in volatile concentrations in the melt at the time of apatite crystallisation, except for lower F in the evolved gabbrodioritic melt compared to the F-rich porphyry-forming and rhyodacitic melts. This may imply that F-rich melts may enhance fluid-rock interaction and facilitate the mineralisation of metal-bearing fluids at the magmatic-hydrothermal transition. Finally, we use apatite chemistry as an independent proxy to interpret evolving fluid salinity and retrieve instantaneous and bulk salinities that are consistent with independent analysis of fluid inclusions in porphyry systems.

## CRedit authorship contribution statement

**C. Lormand:** Conceptualization, Formal analysis, Methodology, Software, Visualization, Writing – original draft, Writing – review & editing. **M.C.S. Humphreys:** Conceptualization, Funding acquisition, Methodology, Resources, Supervision, Validation, Writing – review & editing. **D.J. Colby:** Data curation, Methodology, Software, Writing – review & editing, Formal analysis. **J.P. Coumans:** Formal analysis, Methodology, Software, Writing – review & editing. **C. Chelle-Michou:** Formal analysis, Resources, Validation, Writing – review & editing. **W. Li:** Resources, Validation, Writing – review & editing.

## Declaration of competing interest

The authors declare that they have no known competing financial interests or personal relationships that could have appeared to influence the work reported in this paper.

## Data availability

The Apatite Crystallisation Multistart MATLAB model and the associated files can be accessed on a Durham University repository: STEMMS Apatite Model - Collections ([durham.ac.uk](https://durham.ac.uk)). The DOI of this repository is: doi:[10.15128/r2p5547r44q](https://doi.org/10.15128/r2p5547r44q). This also includes a standalone application of the model in case the user does not have a MATLAB license.

## Acknowledgments

We thank Franziska Keller and an anonymous reviewer for their useful comments which improved our manuscript, and we acknowledge Greg Shellnut for editorial handling. This work was developed during the Consolidator grant for the STEMMS project (STorage and Eruption of Mushy Magma Systems) awarded to PI M. C. S. Humphreys, and supported by the European Research Council under the European Union's Horizon 2020 research and innovation programme [grant number 864923].

## Appendix A. Supplementary data

Supplementary data to this article can be found online at <https://doi.org/10.1016/j.lithos.2024.107623>.

## References

- Aiuppa, A., Baker, D.R., Webster, J.D., 2009. Halogens in volcanic systems. *Chem. Geol.* 263 (1–4), 1–18. <https://doi.org/10.1016/j.chemgeo.2008.10.005>.
- Audétat, A., 2019. The metal content of magmatic-hydrothermal fluids and its relationship to mineralization potential. *Econ. Geol.* 114, 1033–1056. <https://doi.org/10.5382/econgeo.4673>.
- Audétat, A., Pettke, T., Heinrich, C.A., Bodnar, R.J., 2008. Special paper: the composition of magmatic-hydrothermal fluids in barren and mineralised intrusions. *Econ. Geol.* 103 (5), 877–908.
- Bernard, O., Li, W., Costa, F., Saunder, S.S., Itikarai, I., Sindang, M., Bouvet de Maisonneuve, C., 2022. Explosive-effusive-explosive: the role of magma ascent rates and paths in modulating caldera eruptions. *Geology* 50 (9), 1013–1017. <https://doi.org/10.1130/G50023.1>.
- Blake, S., 1984. Volatile oversaturation during the evolution of silicic magma chambers as an eruption trigger. *J. Geophys. Res.* 89 (B10), 8237–8244.
- Humphreys, M.C.S., Blundy, J.D., Sparks, R.S., 2006. Magma evolution and open-system processes at Shiveluch Volcano: Insights from phenocryst zoning. *J. Petrol.* 47 (12), 2303–2334. <https://doi.org/10.1093/petrology/egl045>.
- Bodnar, R.J., Lecumberri-Sanchez, P., Moncada, D., Steele-Macinnis, M., 2014. Fluid inclusion in hydrothermal ore deposits. *Treat. Geochem.* 13, 119–142.
- Borodulin, G.P., Chevychelov, V.Yu., Zaraysky, G.P., 2009. Experimental study of partitioning of tantalum, niobium, manganese and fluorine between aqueous fluoride fluid and granitic and alkaline melts. *Dokl. Earth Sci.* 427, 868–873.
- Boudreau, A.E., 1995. Some geochemical considerations for platinum-group-element exploration in layered intrusions. *Explor. Min. Geol.* 4, 215–225.
- Boudreau, A.E., McCallum, I.S., 1989. Investigations of the stillwater complex: Part V. Apatites as indicators of evolving fluid composition. *Contrib. Mineral. Petrol.* 102, 138–153.
- Boyce, J.W., Hervig, R.L., 2008. Magmatic degassing histories from apatite volatile stratigraphy. *Geology* 36, 63–66.
- Brahm, R., Zellmer, G.F., Kuritani, T., Coulthard, D., Nakagawa, M., Sakamoto, N., Yurimoto, H., Sato, E., 2021. MushPEC: Correcting post-entrapment processes affecting melt inclusions hosted in olivine antecrysts. *Front. Earth Sci.* 8 <https://doi.org/10.3389/feart.2020.599726>.
- Brookfield, A., Cassidy, M., Weber, G., Popa, R.-G., Bachmann, O., Stock, M.J., 2023. Magmatic volatile content and the overpressure 'sweet spot': Implications for volcanic eruption triggering and style. *J. Volcanol. Geotherm. Res.* 44, 107916 <https://doi.org/10.1016/j.jvolgeores.2023.107916>.
- Candela, P.A., 1986. Towards a thermodynamic model for the halogens in magmatic systems: an application to melt-vapor-apatite equilibria. *Chem. Geol.* 57, 289–301. [https://doi.org/10.1016/0009-2541\(86\)90055-0](https://doi.org/10.1016/0009-2541(86)90055-0).
- Candela, P.A., Holland, H.D., 1984. The partitioning of copper and molybdenum between silicate melts and aqueous fluids. *Geochim. Cosmochim. Acta* 48, 373–380.
- Chelle-Michou, C., Chiaradia, M., 2017. Amphibole and apatite insights into the evolution and mass balance of Cl and S in magmas associated with porphyry copper deposits. *Contrib. Mineral. Petrol.* 172, 105. <https://doi.org/10.1007/s00410-017-1417-2>.
- Chelle-Michou, C., Rottier, B., 2021. Transcrustal magmatic controls on the size of porphyry Cu systems: state of knowledge and open questions. *SEG Spec. Publ.* 24, 87–100.
- Chelle-Michou, C., Chiaradia, M., Ovtcharova, M., Ulianov, A., Wotzlav, J.-F., 2014. Zircon petrochronology reveals the temporal link between porphyry systems and the magmatic evolution of their hidden plutonic roots (the Eocene Corocohuayco deposit, Peru). *Lithos* 198–199, 129–140. <https://doi.org/10.1016/j.lithos.2014.03.017>.
- Chelle-Michou, C., Chiaradia, M., Béguelin, P., Ulianov, A., 2015a. Petrological evolution of the magmatic suite associated with the Corocohuayco Cu–Au–Fe Porphyry–skarn deposit, Peru. *J. Petrol.* 56, 1829–1862. <https://doi.org/10.1093/petrology/egv056>.
- Chelle-Michou, C., Chiaradia, M., Selby, D., Ovtcharova, M., Spikings, R.A., 2015b. High-resolution geochronology of the Corocohuayco Porphyry–skarn deposit, Peru: a rapid product of the incaic orogeny. *Econ. Geol.* 110, 423–443. <https://doi.org/10.2113/econgeo.110.2.423>.
- Chevychelov, V.Y., Botcharnikov, R.E., Holtz, F., 2008a. Experimental study of chlorine and fluorine partitioning between fluid and subalkaline basaltic melt. *Dokl. Earth Sci.* 422, 1089–1092.
- Chevychelov, V.Y., Botcharnikov, R.E., Holtz, F., 2008b. Experimental study of fluorine and chlorine contents in mica (biotite) and their partitioning between mica, phonolite melt and fluid. *Geochem. Int.* 46, 1081–1089.
- Chiaradia, M., Caricchi, L., 2017. Stochastic modelling of deep magmatic controls on porphyry copper deposit endowment. *Sci. Rep.* 7, 44523. <https://doi.org/10.1038/srep44523>.
- Dixon, L., Szegő, G.P., 1978. The global optimization problem: an introduction. In: Dixon, L.C.W., Szegő, G.P. (Eds.), *Towards Global Optimisation 2*. North Holland Publishing Company, New York, pp. 1–15.
- Dolejš, D., Zajac, Z., 2018. Halogens in silicic magmas and their hydrothermal systems. In: Harlov, D.E., Aranovich, L. (Eds.), *The Role of Halogens in Terrestrial and Extraterrestrial Geochemical Processes*. Springer Geochemistry. [https://doi.org/10.1007/978-3-319-61667-4\\_7](https://doi.org/10.1007/978-3-319-61667-4_7).
- Evans, K.A., Tomkins, A.G., 2020. Metamorphic fluids in orogenic settings. *Elements* 16, 381–387.
- Gavrilenko, M., Krawczynski, M., Ruprecht, P., Li, W., Catalano, J.G., 2019. The quench control of water estimates in convergent margin magmas. *Am. Mineral.* 104, 936–948. <https://doi.org/10.2138/am-2019-6735>.
- Gibson, S.A., Rooks, E.E., Day, J.A., Petrone, C.M., Leat, P.T., 2020. The role of sub-continental mantle as both “sink” and “source” in deep Earth volatile cycles. *Geochim. Cosmochim. Acta* 275, 140–162. <https://doi.org/10.1016/j.gca.2020.02.018>.
- Giesting, P.A., Filiberto, J., 2014. Quantitative models linking igneous amphibole composition with magma Cl and OH content. *Am. Mineral.* 99, 852–865.
- Glover, F., 1998. A template for scatter search and path relinking. In: Hao, J.-K., Ronald, E., Schoenauer, M., Snyers, S. (Eds.), *Artificial Evolution*. Lecture Notes in Computer Science, 1363. Springer, Berlin/Heidelberg, pp. 13–54.
- Hammouda, T., Chantel, J., Devidal, J.L., 2010. Apatite solubility in carbonatitic liquids and trace element partitioning between apatite and carbonatites at high pressure. *Geochim. Cosmochim. Acta* 24, 7220–7235.
- Harrison, T.M., Watson, E.B., 1984. The behaviour of apatite during crustal anatexis: equilibrium and kinetic considerations. *Geochim. Cosmochim. Acta* 48, 1467–1477.
- Hedenquist, J.W., Lowenstern, J.B., 1994. The role of magmas in the formation of hydrothermal ore deposits. *Nature* 370, 59–527.
- Heinrich, C.A., 2007. Fluid-fluid interactions in magmatic-hydrothermal ore formation. *Rev. Mineral. Geochem.* 65 (1), 363–387. <https://doi.org/10.2138/rmg.2007.65.11>.
- Hogg, O.R., Edmonds, M., Blundy, J., 2023. Water-rich magmas optimise volcanic chalcophile element outgassing fluxes. *Earth Planet. Sci. Lett.* 611, 118153. <https://doi.org/10.1016/j.epsl.2023.118153>.
- Hughes, J., 2015. Presidential Address. The many facets of apatite. *Am. Mineral.* 100 (5–6), 1033–1039. <https://doi.org/10.2138/am-2015-5193>.
- Hughes, J.M., Nekvasil, H., Ustunisik, G., Lindsley, D.H., Coraor, A.E., Vaughn, J., Phillips, B.L., McCubbin, F.M., Woerner, W.R., 2014. Solid solution in the fluorapatite-chlorapatite binary system: High-precision crystal structure refinements of synthetic F-Cl apatite. *Am. Mineral.* 99 (2–3), 369–376.
- Humphreys, M.C.S., Smith, V.C., Coumans, J.P., Riker, J.M., Stock, M.J., de Hoog, J.C.M., Brooker, R.A., 2021. Rapid pre-eruptive mush reorganisation and atmospheric volatile emissions from the 12.9 ka Laacher See eruption, determined using apatite. *Earth Planet. Sci. Lett.* 576, 117198. <https://doi.org/10.1016/j.epsl.2021.117198>.
- Humphreys, M.C.S., Smith, V.C., Lormand, C., Coumans, J.P., Brooker, R.A., Stock, M.J., 2022. The apatite record of pre-eruptive magma mixing and mush disaggregation. *Goldschmidt*. <https://doi.org/10.46427/gold2022.11402>, 2022 abstract.
- Iveson, A.A., Webster, J.D., Rowe, M.C., Neill, O.K., 2017. Major element and halogen (F, Cl) mineral–melt–fluid partitioning in hydrous rhyodacitic melts at shallow crustal conditions. *Journal of Petrol.* 58 (12), 2465–2492. <https://doi.org/10.1093/petrology/egy011>.
- Kouzmanov, K., Pokrovski, G.S., 2012. Hydrothermal controls on metal distribution in porphyry Cu (Mo–Au) systems. *Soc. Econ. Geol. Spec. Publ.* 16, 573–618. <https://doi.org/10.5382/SP.16.22>.
- Krause, J., Harlov, D.E., Pushkarev, E.V., Brüggemann, G.E., 2013. Apatite and clinopyroxene as tracers for metasomatic processes in nepheline clinopyroxenites of Uralian-Alaskan-type complexes in the Ural Mountains, Russian federation. *Geochim. Cosmochim. Acta* 121, 503–521. <https://doi.org/10.1016/j.gca.2013.06.013>.
- Lamy-Chappuis, B., Heinrich, C.A., Driesner, T., Weis, P., 2020. Mechanisms and patterns of magmatic fluid transport in cooling hydrous intrusions. *Earth Planet. Sci. Lett.* 535, 116111.
- Lange, R.A., Frey, H.M., Hektor, J., 2009. A thermodynamic model for the plagioclase-liquid hygrometer/thermometer. *Am. Mineral.* 94 (4), 494–506.
- Lecumberri-Sanchez, P., Bodnar, R.J., 2018. Halogen geochemistry of ore deposits: contributions towards understanding sources and processes. In: Harlov, D., Aranovich, L. (Eds.), *The Role of Halogens in Terrestrial and Extraterrestrial*

- Geochemical Processes. Springer Geochemistry. Springer, Cham. [https://doi.org/10.1007/978-3-319-61667-4\\_5](https://doi.org/10.1007/978-3-319-61667-4_5).
- Li, W., Costa, F., 2020. A thermodynamic model for F-Cl-OH partitioning between silicate melts and apatite including non-ideal mixing with application to con-straining melt volatile budgets. *Geochim. Cosmochim. Acta* 269, 203–222. <https://doi.org/10.1016/j.gca.2019.10.035>.
- Li, W., Costa, F., 2023. Corrigendum to “A thermodynamic model for F-Cl-OH partitioning between silicate melts and apatite including non-ideal mixing with application to constraining melt volatile budgets”. *Geochim. Cosmochim. Acta* 269 (2020), 203–222. *Geochim. Cosmochim. Acta* 347, 125. <https://doi.org/10.1016/j.gca.2023.02.010>.
- Li, W., Costa, F., Nagashima, K., 2021. Apatite Crystals Reveal Melt Volatile Budgets and Magma Storage Depths at Merapi Volcano, Indonesia. *J. Petrol.* 62 (4), ega100. <https://doi.org/10.1093/ptrology/egaa100>.
- Li, H., Hermann, J., 2017. Chlorine and fluorine partitioning between apatite and sediment melt at 2.5 GPa, 800 C: a new experimentally derived thermodynamic model. *Am. Mineral.* 102 (3), 580–594.
- Li, W., Chakraborty, S., Nagashima, K., Costa, F., 2020a. Multicomponent diffusion of F, Cl and OH in apatite with application to magma ascent rates. *Earth Planet. Sci. Lett.* 550, 116545 <https://doi.org/10.1016/j.epsl.2020.116545>.
- Li, W., Costa, F., Nagashima, K., 2020b. Apatite crystals reveal melt volatile budgets and magma storage depths at Merapi volcano, Indonesia. *J. Petrol.* 62 (4), ega100.
- McPhie, J., Kamenetsky, V., Allen, S., Ehrig, K., Agangi, A., Bath, A., 2011. The fluorine link between a supergiant ore deposit and a silicic large igneous province. *Geology* 39 (11), 1003–1006. <https://doi.org/10.1130/G32205.1>.
- Metrich, N., Clocciatti, R., 1989. Melt inclusion investigation of the volatile behaviour in historic alkali basaltic magmas of Etna. *Bull. Volcanol.* 51, 185–198.
- Nathwani, C.L., Wilkinson, J.J., Brownscombe, W., John, C.M., 2023. Mineral texture classification using deep convolutional neural networks: an application to zircons from porphyry copper deposits. *J. Geophys. Res. Solid Earth* 128. <https://doi.org/10.1029/2022JB025933>.
- Pamukcu, A.S., Gualda, G.A.R., Bégue, F., Gravelly, D.M., 2015. Melt inclusion shapes: Timekeepers of short-lived giant magma bodies. *Geology* 43 (11), 947–950. <https://doi.org/10.1130/G37021.1>.
- Piccoli, P., Candela, P., 1994. Apatite in felsic rocks; a model for the estimation of initial halogen concentrations in the Bishop Tuff (Long Valley) and Tuolumne Intrusive Suite (Sierra Nevada Batholith) magmas. *Am. J. Sci.* 294 (1), 92–135.
- Popa, R.G., Tollan, P., Bachmann, O., Schenker, V., Ellis, B., Allaz, J.M., 2021. Water exsolution in the magma chamber favors effusive eruptions: Application of Cl-F partitioning behavior at the Nisyros-Yali volcanic area. *Chem. Geol.* 570, 120170.
- Richards, J., 2015. The oxidation state, and sulfur and Cu contents of arc magmas: implications for metallogeny. *Lithos* 233, 27–45. <https://doi.org/10.1016/j.lithos.2014.12.011>.
- Richards, J.P., 2022. Porphyry copper deposit formation in arcs: what are the odds? *Geosphere* 18 (1), 130–155.
- Ridolfi, F., Renzulli, A., 2012. Calcic amphiboles in calc-alkaline and alkaline magmas: thermobarometric and chemometric empirical equations valid up to 1130°C and 2.2 Gpa. *Contrib. Mineral. Petrol.* 163, 877–895. <https://doi.org/10.1007/s00410-011-0704-6>.
- Riker, J., Humphreys, M.C.S., Brooker, R.A., De Hoog, J.C., EIMF, 2018. First measurements of OH-C exchange and temperature-dependent partitioning of OH and halogens in the system apatite-silicate melt. *Am. Mineral.* 103 (2), 260–270.
- Schipper, B.W., Lin, H.C., Meloni, M.A., Wansleben, K., Heijungs, R., van der Voet, E., 2018a. Estimating global copper demand until 2100 with regression and stock dynamics. *Resour. Conserv. Recycl.* 132, 28–36. <https://doi.org/10.1016/j.resconrec.2018.01.004>.
- Schöpa, A., Annen, C., Dilles, J.H., Sparks, R.S.J., Blundy, J.D., 2017. Magma emplacement rates and porphyry copper deposits: thermal modeling of the Yerington Batholith, Nevada. *Econ. Geol.* 112 (7), 1653–1672 (Shannon & Prewitt (1969)).
- Scott, J.A., Humphreys, M.C.S., Mather, T.A., Pyle, D.M., Stock, M.J., 2015. Insights into the behaviour of S, F, and Cl at Santiaguito Volcano, Guatemala, from apatite and glass. *Lithos* 232, 375–394.
- Shannon, R.D., Prewitt, C.T., 1969. Effective ionic radii in oxides and fluorides. *Acta Cryst B25*, 925–946. <https://doi.org/10.1107/S0567740869003220>.
- Shinohara, H., Hedenquist, J.W., 1997. Constraints on Magma Degassing beneath the far southeast porphyry Cu–Au deposit, Philippines. *J. Petrol.* 38 (12), 1741–1752. <https://doi.org/10.1093/ptroj/38.12.1741>.
- Simon, A.C., Ripley, E.M., 2011. The role of magmatic sulfur in the formation of ore deposits. *Rev. Mineral. Geochem.* 73 (1), 513–578.
- Stock, M.J., Humphreys, M.C.S., Smith, V.C., Isaia, R., Brooker, R.A., Pyle, D.M., 2016. Late-stage volatile saturation as a potential trigger for explosive volcanic eruptions. *Nat. Geosci.* 9, 249–254. <https://doi.org/10.1038/ngeo2639>.
- Stock, M.J., Humphreys, M.C.S., Smith, V.C., Isaia, R., Brooker, R.A., Pyle, D.M., 2018. Tracking volatile behaviour in sub-volcanic plumbing systems using apatite and glass: insights into pre-eruptive processes at Campi Flegrei, Italy. *J. Petrol.* 59 (12), 2463–2492.
- Tattitch, Brian C., Blundy, J., 2017. Cu-Mo partitioning between felsic melts and saline-aqueous fluids as a function of  $X_{\text{NaCl}_{\text{aq}}}$ ,  $f_{\text{O}_2}$ , and  $f_{\text{S}_2}$ . *Am. Mineral.* 102 (10), 1987–2006. <https://doi.org/10.2138/am-2017-5998>.
- Tattitch, B., Chelle-Michou, C., Blundy, J., Loucks, R.R., 2021. Chemical feedbacks during magma degassing control chlorine partitioning and metal extraction in volcanic arcs. *Nat. Commun.* 12 (1), 1774. <https://doi.org/10.1038/s41467-021-21887-w>.
- Watson, E.B., Green, T.H., 1981. Apatite/liquid partition coefficients for the rare earth elements and strontium. *Earth Planet. Sci. Lett.* 56, 405–421.
- Webster, J.D., Tappen, C.M., Mandeville, C.W., 2009. Partitioning behavior of chlorine and fluorine in the system apatite–melt–fluid. II: Felsic silicate systems at 200 MPa. *Geochim. Cosmochim. Acta* 73 (3). <https://doi.org/10.1016/j.gca.2008.10.034>.
- Wilkinson, J.J., 2013. Triggers for the formation of porphyry ore deposits in magmatic arcs. *Nat. Geosci.* 6 (11), 917–925.
- Xing, Y., Etschmann, B., Liu, W., Mei, Y., Shvarov, Y., Testemale, D., Tomkins, A., Brugger, J., 2019. The role of fluorine in hydrothermal mobilization and transportation of Fe, U and REE and the formation of IOCG deposits. *Chem. Geol.* 504, 158–176. <https://doi.org/10.1016/j.chemgeo.2018.11.008>.
- Zajacz, Z., Candela, P.A., Piccoli, P.M., Wälle, M., Sanchez-Valle, C., 2012. Gold and copper in volatile saturated mafic to intermediate magmas: Solubilities, partitioning, and implications for ore deposit formation. *Geochim. Cosmochim. Acta* 91, 140–159.
- Zhang, C., Holtz, F., Ma, C., Wolff, P.E., Li, X., 2012. Tracing the evolution and distribution of F and Cl in plutonic systems from volatilebearing minerals: a case study from the Liujiaawa pluton (Dabie orogen, China). *Contrib. Mineral. Petrol.* 164, 859–879. <https://doi.org/10.1007/s00410-012-0778-9>.
- Zsolt, U., Lasdon, L., Plummer, J.C., Glover, R., Kelly, J., Martí, R., 2007. Scatter search and local NLP solvers: a multistart framework for global optimization. *INFORMS J. Comput.* 19 (3), 328–340.